

## Developing energy-efficient nitrate-to-ammonia flow cells with bifunctional NiFeW-oxide thin-film electrodes made by magnetron sputtering technique

Quoc-Nam Ha <sup>a</sup>, Wen-Chuan Hsiao <sup>a</sup>, Yu-Chan Chan <sup>b</sup>, Tadele Negash Gemedo <sup>a</sup>, Merga Hailemariam Urgesa <sup>a</sup>, Dong-Hau Kuo <sup>a,b,\*</sup>

<sup>a</sup> Department of Materials Science and Engineering, National Taiwan University of Science and Technology, #43, Section 4, Keelung Road, Taipei 10607, Taiwan

<sup>b</sup> Graduate Institute of Energy and Sustainability Technology, National Taiwan University of Science and Technology, #43, Section 4, Keelung Road, Taipei 10607, Taiwan

### ARTICLE INFO

#### Keywords:

Electrocatalytic nitrate reduction  
NiFeW-oxide  
Oxygen vacancy  
Energy consumption  
Energy efficiency

### ABSTRACT

Herein, we develop a sputtered NiFeW-oxide thin-film bifunctional electrocatalyst with the incorporated oxygen vacancies and multivalent cations of  $\text{Ni}^{2+}/\text{3+}$ ,  $\text{Fe}^{2+}/\text{3+}$ , and  $\text{W}^{6+}$  to enhance the economic viability of electrocatalytic nitrate reduction for commercial applications. Our NFW-0.5 achieves a notable  $54.6 \text{ mg/h.cm}^2$  ammonia yield rate at a modest applied potential of  $-0.2 \text{ V vs. RHE}$ , coupled with an outstanding Faradaic efficiency of 93.7%. Furthermore, our NFW-0.5(+)||NFW-0.5(−) flow-cell electrolyzer with a larger electrode of  $2 \times 2 \text{ cm}^2$  reveals an impressive ammonia productivity of  $143.5 \text{ mg/h.cm}^2$  at a cell voltage of  $2.0 \text{ V}$ , accompanied by a superior Faradaic efficiency of 96.1%, an energy efficiency of 26%, and a low energy consumption of  $26.3 \text{ kWh/kg.NH}_3$ . An oxygen vacancy-based  $\text{NO}_3$ -pinned mechanism is proposed to explain our excellent nitrate reduction. Our work introduces a new paradigm to design efficient and bifunctional electrocatalysts for potential industrial-scale ammonia production.

### 1. Introduction

Ammonia ( $\text{NH}_3$ ) assumes a critical role in the nitrogen cycle network and stands as a pivotal compound in various industrial applications, such as the synthesis of fertilizers, explosives, and plastics [1]. Traditionally, its production relied on the energy-intensive Haber–Bosch process, utilizing dinitrogen ( $\text{N}_2$ ) and hydrogen ( $\text{H}_2$ ) as feedstocks, imposing harsh reaction conditions with temperatures ranging from 400 to  $450^\circ\text{C}$  and pressures between 5 and 25 MPa, and significantly contributing to global energy consumption and greenhouse gas emissions [2].

In recent years, there has been a burgeoning interest in the nitrogen reduction reaction ( $\text{N}_2\text{RR}$ ) for ammonia synthesis. The electrochemical  $\text{N}_2\text{RR}$  has emerged as a promising alternative to the Haber–Bosch process, owing to the abundance of raw materials and environmentally friendly synthesis conditions. Despite its potential benefits, the electrochemical reduction of nitrogen gas encounters challenges. The limited solubility and high ionization energy of  $\text{N}_2$ , arising from its nonpolar molecular

structure and a robust triple bond ( $\approx 941 \text{ kJ/mol}$ ), lead to the low activity and selectivity of current electrocatalysts for  $\text{N}_2$  reduction [3,4].

More recently, the nitrate reduction reaction ( $\text{NO}_3\text{RR}$ ) has garnered attention, primarily owing to the lower dissociation energy of the  $\text{N=O}$  bond ( $204 \text{ kJ/mol}$ ), indicating its potential for a high ammonia yield [5]. Various catalyst systems have proven to be effective for  $\text{NO}_3\text{RR}$ , including metals [6,7], metal oxides [8,9], metal sulfides [10,11], and metal phosphides [12,13]. Di Liu *et al.* [14] investigated Mn-substituted  $\text{Co}_3\text{O}_4$  nanotubes, which exhibited an excellent ammonia yield rate of  $35 \text{ mg/h.cm}^2$  and a high Faradaic efficiency (FE) exceeding 99.5% at  $-1.2 \text{ V}$  versus reversible hydrogen electrode (vs. RHE) under ambient conditions. Hollow  $\text{Cu}_2\text{O}$  h-NCs exhibited outstanding  $\text{NO}_3\text{RR}$  activities, achieving a remarkable  $56.2 \text{ mg/h.mg}_{\text{cat}}$  and an FE of 92.9% at an applied potential of  $-0.85 \text{ V}$  vs. RHE [15]. In a more recent development, nearly 100% Faraday efficiency for  $\text{NO}_3\text{RR}$  at a high current density has been achieved by utilizing copper-dispersed todorokite-type manganese oxide. This system attained a yield rate of  $0.51 \text{ mmol/h.cm}^2$  at  $-1.2 \text{ V}$  vs. RHE [16].

\* Corresponding author at: Department of Materials Science and Engineering, National Taiwan University of Science and Technology, #43, Section 4, Keelung Road, Taipei 10607, Taiwan.

E-mail address: [dhkuo@mail.ntust.edu.tw](mailto:dhkuo@mail.ntust.edu.tw) (D.-H. Kuo).



While current catalysts have achieved high Faradaic efficiency (> 90%) and valuable production rates, they require excessive overpotentials exceeding -0.5 V vs RHE. These elevated overpotentials not only result in energy loss but also foster the competitive hydrogen evolution reaction (HER), reducing the Faradaic efficiency of NH<sub>3</sub> and compromising energy efficiency (EE) for NO<sub>3</sub>RR. The NO<sub>3</sub>RR process is complicated, involving the transfer of 9 protons and 8 electrons. The high overpotential observed can be attributed to the sluggish rate-determining step in the electroreduction of nitrate to nitrite [17]. This presents an obstacle in the design and synthesis of cutting-edge electrocatalysts. Overcoming this challenge is crucial for fostering the evolution of high-performance NO<sub>3</sub>RR catalysts. Strategies for achieving high performance include the incorporation of vacancies, fine-tuning of electronic structures, enhancement of electron accumulation and depletion, as well as modulation of the chemical environment [18,19]. These advancements are essential for developing efficient NO<sub>3</sub>RR electrocatalysts. Furthermore, the electrochemical reaction involves cathode reduction i.e., NO<sub>3</sub>RR, and anode oxidation e.g., oxygen evolution reaction (OER). The OER is a kinetically unfavorable process requiring a high standard oxidation potential (1.23 V vs. RHE), inevitably increasing the overall operation potential and diminishing the energy efficiency of ammonia production. To facilitate and simplify ammonia production through nitrate electrolysis, a bifunctional catalyst demonstrating high activity for both NO<sub>3</sub>RR and OER is imperative. Additionally, evaluating NO<sub>3</sub>RR in a practical flow-cell electrolyzer will provide a more comprehensive assessment of feasibility for industrial applications.

NiFe-based electrocatalysts have garnered significant attention for applications in NO<sub>3</sub>RR, OER, and other electrochemical processes. This is primarily due to their exceptional electrical conductivity and impressive catalytic activity. The presence of iron (Fe) active sites provides moderate adsorption capacity for oxygen and nitrogen atoms [20], while nickel (Ni) active sites contribute to the generation of active hydrogen intermediates, thereby playing a crucial role in improving NO<sub>3</sub>RR performance [21]. NiFe-based catalysts have also demonstrated distinct catalytic activity for OER, often attributed to their self-reconstructed amorphous phase or (oxy)hydroxides formed on the surface under anodic potential [22]. Besides, multi-cation oxide systems containing oxygen vacancies (OVs) have been identified as promising candidates for capturing and converting reaction species, owing to their electron accumulation and charge-transport behavior [23]. Therefore, designing multi-metal/metal oxide systems based on NiFe-based catalysts with defective oxygen sites may represent a promising strategy for achieving bifunctional electrocatalysts capable of facilitating both NO<sub>3</sub>RR at the anode and OER at the cathode in a single cell effectively.

This study introduces, for the first time, a bifunctional NiFeW-oxide thin-film electrocatalyst fabricated by the magnetron sputtering technique, specifically designed to enhance both the efficiencies of NO<sub>3</sub>RR and OER. The amorphous NiFeW-oxide deposit contains a metallic alloy of Ni, Fe, and W, and a partially oxidized metal oxide with multi-valent cations and oxygen vacancies for functionality. The collective findings from electron paramagnetic resonance (EPR), X-ray photoelectron spectroscopy (XPS), *in-situ* Raman, and *operando* electrochemical impedance spectroscopy (EIS) elucidate the pivotal role of OVs in facilitating more efficient charge transport and lowering the overpotential, leading to the heightened activity of the NFW-oxide catalyst. Through adjustment of the target composition, our NFW-0.5 catalyst, featuring a Ni: Fe: W ratio of 1: 1: 0.5, demonstrates exemplary NO<sub>3</sub>RR and OER performance. The feasibility of our NFW-0.5(+)||NFW-0.5(−) stack cell was thoroughly evaluated. We also provided information on energy efficiency and energy consumption to offer a more comprehensive understanding of the electrocatalyst's effectiveness in ammonia production—an aspect that is seldom considered in most recent NO<sub>3</sub>RR studies.

## 2. Experimental section

### 2.1. Fabrication of sputtered NiFeW-oxide thin film electrodes

The ternary NiFeW-oxide sputtering targets were produced using a custom-made hot-press apparatus. In a concise overview, a zirconium ball milling process was employed to meticulously homogenize a mixture of powdered Ni, Fe, and W with varying tungsten ratios (Ni<sub>1</sub>Fe<sub>1</sub>W<sub>0.25</sub>, Ni<sub>1</sub>Fe<sub>1</sub>W<sub>0.5</sub>, and Ni<sub>1</sub>Fe<sub>1</sub>W<sub>1</sub>). Subsequently, the thoroughly blended powder was meticulously placed into a graphite mold, which included a copper plate for additional support. The mold was then introduced into the hot-press machine chamber, where a hot-pressing procedure was conducted under 300 psi of hydraulic pressure for 30 min at 450 °C. Following this, the target was carefully demolded and, after naturally cooling, underwent polishing with sandpaper.

### 2.2. Fabrication of ternary NiFeW-oxide sputtering targets

In the deposition process outlined in **Scheme 1**, the sputtering chamber underwent a sequential evacuation procedure. Initially, it was evacuated to achieve a low vacuum state using a rotary pump, followed by further evacuation to achieve a high vacuum state using a turbo molecular pump for 1 h until a pressure of 10<sup>-6</sup> torr was reached. Subsequently, a pre-sputtering step was conducted using a low power of 50 watts for approximately 30 min to eliminate surface contaminants. The target, positioned at a working distance of 4 cm, underwent sputtering at a temperature of 200 °C, employing a power of 70 W for 30 min. Throughout the sputtering process, argon gas was used as the operational gas at a pressure of 9.5 × 10<sup>-3</sup> torr.

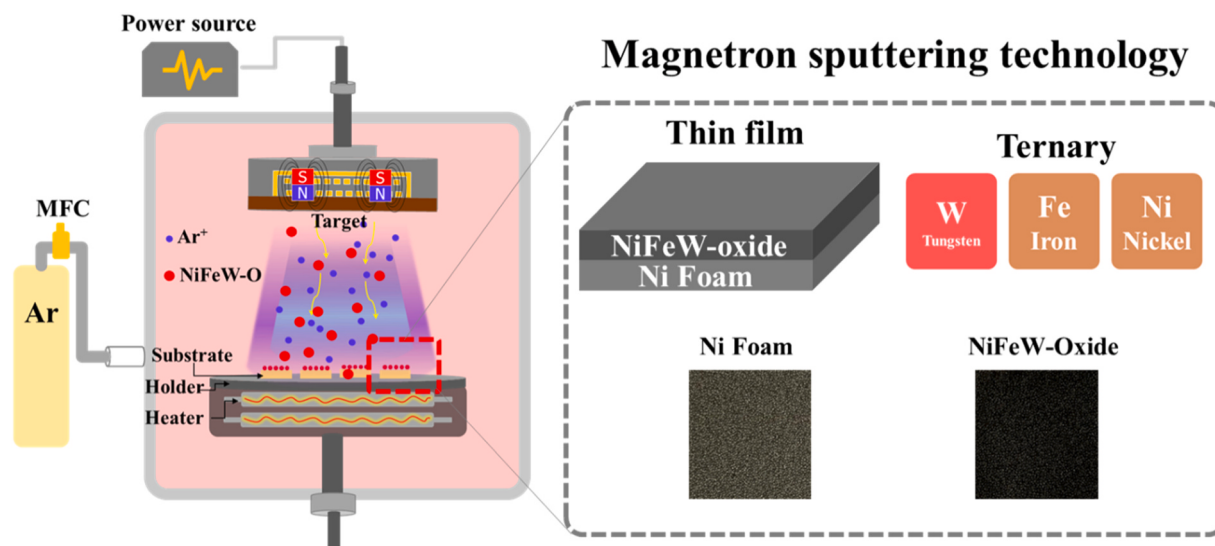
Depending on the specific sputtering targets utilized, such as Ni<sub>1</sub>Fe<sub>1</sub>W<sub>0.25</sub>, Ni<sub>1</sub>Fe<sub>1</sub>W<sub>0.5</sub>, and Ni<sub>1</sub>Fe<sub>1</sub>W<sub>1</sub>, the resulting as-sputtered samples were labeled as NFW-0.25, NFW-0.5, and NFW-1.0, respectively. Additionally, a single Ni and binary NiFe catalyst were synthesized using the same methodology, excluding tungsten from the mixture for comparative purposes.

### 2.3. Characterizations

The crystal structures of the as-sputtered NiFeW-oxide thin films were investigated using a Bruker D2 Phaser X-ray Diffractometer with Cu-Kα radiation (35 kV, 20 mA,  $\lambda = 1.5184 \text{ \AA}$ ). Morphological analysis was conducted using a high-resolution field-emission scanning electron microscope (SEM, JEOL JMS-6500 F) at an accelerating voltage of 15 kV. Transmission electron microscopy (TEM) and energy dispersive X-ray spectroscopy (EDS) were performed using the FEI Talos F200X at an operating voltage of 200 kV. The surface chemical oxidation states of individual elements were determined via X-ray photoelectron spectroscopy (XPS, VG Scientific ESCALAB 250). Electron Paramagnetic Resonance (EPR) spectra were recorded using a Bruker EPR-plus spectrometer.

### 2.4. Electrochemical measurements

All electrochemical measurements were carried out using a BioLogic SP-300 potentiostat. To investigate the nitrate reduction reaction, we employed a three-electrode H-cell system with the following components: the as-prepared NiFeW-oxide ( $1 \times 1 \text{ cm}^2$ ) as the working electrode, a platinum foil as the counter electrode, and a Hg/HgO electrode as the reference electrode. The electrolytes consisted of 1 M KOH with varying concentrations of KNO<sub>3</sub>. To ensure consistency, all reported potentials were adjusted to the Reversible Hydrogen Electrode (RHE) using the Nernst equation [24]. Linear Sweep Voltammetry (LSV) experiments were conducted to assess performance within a potential window ranging from -0.4–0 V vs. RHE at a sweep rate of 5 mV/s. Additionally, electrochemical double-layer capacitance (C<sub>dl</sub>) was estimated through cyclic voltammetry (CV) measurements at different scan



**Scheme 1.** Fabrication procedure of partially oxidized NiFeW-oxide thin film catalyst.

rates, ranging from 20 to 100 mV. Electrochemical impedance spectroscopy (EIS) was performed at various applied potentials versus RHE in the frequency range from 100 mHz to 200 kHz. For the overall electrolytic ammonia production test, a two-electrode system was utilized, where the best catalyst for NO<sub>3</sub>RR and OER served as both anode and cathode electrodes ( $2 \times 2 \text{ cm}^2$ ), with the current density normalized to the geometric electrode area of 1 cm<sup>2</sup>.

To explore the active components of NiFeW-oxide during the NO<sub>3</sub>RR, *in-situ* Raman analysis was conducted using a confocal Raman spectrometer (HORIBA, LabRAM HR evolution) with an excitation wavelength of 532 nm. Prior to the experiment, calibration of the Raman frequency was performed using a Si wafer (520.7 cm<sup>-1</sup>). For the electrochemical tests, a custom-made three-electrode electrochemical cell was employed. In this configuration, the as-prepared NFW-0.5 sample

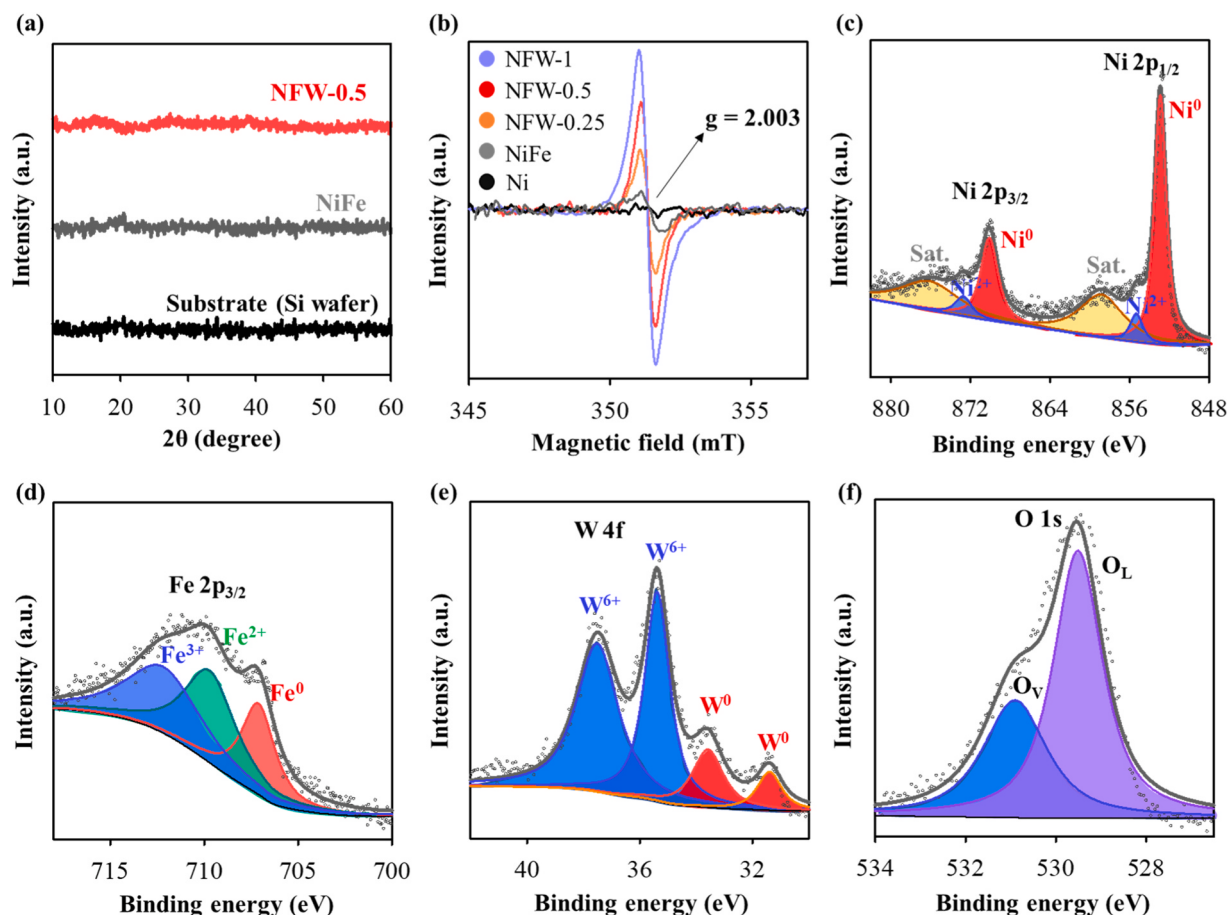


**Fig. 1.** (a) X-ray diffraction spectra and (b) electron paramagnetic resonance spectra of as-sputtered thin films. High-resolution XPS spectra of (c) Ni 2p, (d) Fe 2p, (e) W 4f, and (f) O 1s for NFW-0.5.

served as the working electrode ( $1 \times 1 \text{ cm}^2$ ), accompanied by a platinum foil as the counter electrode and a Hg/HgO reference electrode. External bias was applied to the working electrode during Raman analysis using the potentiostat (BioLogic, SP-300). Potential-dependent Raman spectroscopy was conducted under open-circuit conditions or during potentiostatic electrolysis, employing chronoamperometry in a 1 M KOH electrolyte or 1 M KOH + 100 mM KNO<sub>3</sub>. Distinctly applied potentials ranging from 0.1 to -0.3 V vs. RHE were studied to explore the oxidation stages changed in NFW-0.5 during the NO<sub>3</sub>RR process.

The experiments to capture active hydrogen intermediate (H<sub>ad,\*</sub>) were conducted in electrolytes both with and without KNO<sub>3</sub>, utilizing 5,5-dimethyl-1-pyrroline N-oxide (DMPO) as the capturing agent. In details, the cathode area was set to  $1 \times 1 \text{ cm}^2$ , and the electrolyte volume was maintained at 25 mL. After undergoing a 10 min reaction under the applied cathodic potential, 1.5 mL of electrolyte was withdrawn and combined with 0.5 mL of DMPO (50 mM). The resulting mixture was then transferred to a capillary tube for detection using a Bruker EPR-plus spectrometer.

### 3. Results and discussion

#### 3.1. Electrocatalyst characterizations

The evaluation of the crystal structure of the sputtered NiFeW-oxide thin film was conducted by X-ray diffraction (XRD) analysis. As presented in Fig. 1a, both NiFe and NFW-0.5 exhibit XRD patterns devoid of distinct peaks resembling the substrate spectrum. This result strongly suggests the amorphous nature of the as-prepared binary NiFe and ternary NiFeW-oxide thin films. The element oxidation states of NFW-0.5 were scrutinized by utilizing X-ray photoelectron spectroscopy (XPS). The high-resolution Ni 2p regions, illustrated in Fig. 1c, display

two main peaks for Ni 2p<sub>3/2</sub> and Ni 2p<sub>1/2</sub>, which could be further deconvoluted into four subpeaks corresponding to the binding energies of Ni<sup>0</sup> (852.9 and 870.1 eV) and Ni<sup>2+</sup> (855.3 and 872.7 eV) [25–27]. Based upon the absorption coefficient and the peak integration, 16.7% for Ni<sup>2+</sup> and 83.3% for Ni metal were obtained. In the Fe 2p spectrum (Fig. 1d), the deconvoluted peaks at 707.1, 709.7, and 712.2 eV distinctly correspond to the 2p<sub>3/2</sub> binding energies of Fe<sup>0</sup>, Fe<sup>2+</sup>, and Fe<sup>3+</sup> [28,29], respectively, highlighting the multiple oxidation states of Fe. The Fe<sup>0</sup>: Fe<sup>2+</sup>: Fe<sup>3+</sup> ratio is 0.248: 0.370: 0.382. The high-resolution W 4 f regions (Fig. 1e) further demonstrate the coexistence of W metal (31.4 and 33.6 eV) and W<sup>6+</sup> (35.4 and 37.5 eV) with a high oxidation state in NFW-0.5 [30]. The W<sup>0</sup>: W<sup>6+</sup> ratio is 0.174: 0.826. Furthermore, as illustrated in Fig. 1f, the O 1 s spectrum can be deconvoluted into two peaks at binding energies of 529.5 and 531.1 eV, which are assigned to the lattice oxygen and OVs in the defective oxide with the contents of 64% and 36%, respectively [31]. As illustrated in Fig. 1b, the presence of OVs in NiFe, and NFW-n was supported by Electron Paramagnetic Resonance (EPR) with a signal at g = 2.003, corresponding to electrons trapped at oxygen vacancy sites [32]. Significantly, the OV signal intensity of NFW-0.5 was surpassed for NiFe, indicating that a larger amount of OVs is attributed to the synergistic effect of W substitution into NiFe in NFW-0.5. It further observed that the extent of W substitution directly influenced the formation of OVs. The NFW-1 catalyst, with higher levels of W substitution, exhibited the highest concentration of OVs, while NFW-0.25, with a lower amount of W substitution, displayed fewer OVs. From the XPS analysis, the coating contains the amorphous phases in the (Ni, Fe, W) metallic alloy and metal oxide. As the precursor powders consist of metallic powders, it is notable that a significant amount of oxygen was detected in the Fe powder precursor, as mentioned in our previous work [33]. This oxygen content, originating from the easily oxidized surface of the Fe precursor powder, can

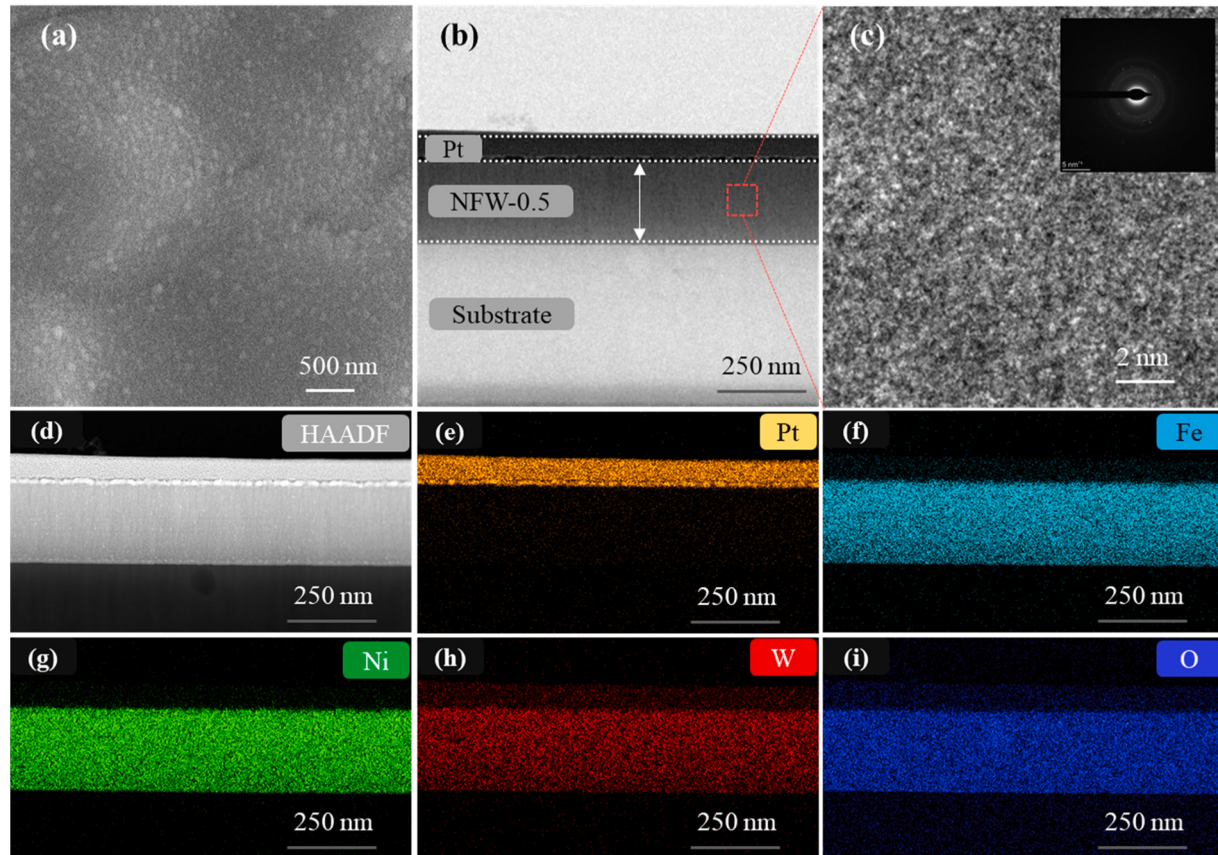


**Fig. 2.** (a) FE-SEM image of NFW-0.5. (b) FE-TEM cross-sectional image and (c) HR-TEM image with the inset for the SAED pattern. (d) HAADF image and elementals mapping images of (e) platinum, (f) nickel, (g) iron, (h) tungsten, and (i) oxygen of NFW-0.5.

partially oxidize other metals such as Ni and W during sputtering. Consequently, the deposited material can be denoted as NiFeW-oxide.

We conducted electron microscopy to evaluate the morphology of our NFW-0.5 electrocatalyst. As shown in Fig. 2a and S2, the main observation from the top-view scanning electron microscopy (SEM) images shows that the sputtered NFW-0.5 film is dense and demonstrates high surface smoothness. Fig. 2b illustrates a representative cross-sectional transmission electron microscopy (TEM) image of NFW-0.5. It is noteworthy that a thin layer of platinum was coated on the surface of the thin film to shield it from ion bombardment during sample preparation (Figs. 2b and 2e). The TEM analysis confirms the continuous and uniform nature of the sputtered film, with an estimated thickness of approximately 250 nm. As depicted in Fig. 2c, a lack of regular atomic arrangement is evident in the high-resolution TEM (HRTEM) image; Moreover, the SAED pattern (insert in Fig. 2c) exhibits a blurred image rather than a clearly defined ring or dot pattern, indicative of the amorphous nature of the thin film, consistent with the XRD results. To examine the distributions of Ni, Fe, W, and O elements, we obtained elemental mapping signals using a scanning transmission electron microscope in a high-angle annular dark-field (HAADF) mode (Fig. 2d). As presented in Fig. 2f-e, a homogeneous dispersion of nickel, iron, tungsten, and oxygen elements was observed throughout the NFW-0.5 thin film. This uniform distribution ensures an even allocation of catalytic active sites across the surface of NFW-0.5 to enhance its potential for catalytic activity [34].

To characterize the metal-oxide phase, EDS compositions of the deposits from the SEM facility are measured, as shown in Table S1. The NFW-0.5 has the Ni:Fe:W:O ratio at 1: 0.91: 0.29: 0.84. To separate the cationic states from the metallic states with the XPS data in Fig. 1, the  $\text{Ni}^{2+}$ : $(\text{Fe}^{2+}+\text{Fe}^{3+})$ : $\text{W}^{6+}$ :anion ratio at 0.14: 0.69: 0.24: 0.84. The molar ratios of the cations of Ni, Fe, and W are 13%, 65%, and 0.22%, respectively. The dominant oxide phase is the iron oxide with the  $\text{Ni}^{2+}$  and  $\text{W}^{6+}$  as the dopants in the lattice. As the  $\text{Fe}^{2+}/\text{Fe}^{3+}$  ratio of ~1, the iron oxide cannot be amorphous  $\text{FeO}$  or  $\text{Fe}_2\text{O}_3$  but the  $\text{Fe}_3\text{O}_4$  phase with the anion: cation ratio of 4: 3 or the anion/cation ratio of 1.33. The anion/cation ratio of our NFW-0.5 is 0.79, so the anion-deficient  $\text{Fe}_3\text{O}_{4-x}$  spinel is formed. The real composition of the amorphous spinel can be expressed as  $(\text{Ni}_{0.14}\text{Fe}_{0.34}\text{Fe}_{0.35}\text{W}_{0.24})\text{O}_{0.84}$ ,  $(\text{Ni}_{0.13}\text{Fe}_{0.32}\text{Fe}_{0.33}\text{W}_{0.22})\text{O}_{1.07}\text{O}_{0.84}$ , or  $(\text{Ni}_{0.13}\text{Fe}_{0.32}\text{Fe}_{0.33}\text{W}_{0.22})\text{O}_3\text{O}_{2.37}$ . In brief, the metal oxide is the partially oxidized NiFeW i.e.,  $(\text{Fe}, \text{Ni}, \text{W})_3\text{O}_{4-x}$ . The deposited film contains metallic alloy of Ni, Fe, and W, and metal oxide of  $(\text{Fe}, \text{Ni}, \text{W})_3\text{O}_{4-x}$ . VO in the highly oxygen-deficient spinel provides the pinning site for the interaction between the electrode and the reactants.

The formation of our partially oxidized NiFeW thin film is expounded as follows: During the magnetron sputtering process, high-energy argon ions bombard the NiFeW target surface. The collision of these ions with target materials imparts their kinetic energy to the target atoms and molecules. Consequently, O atoms mainly from the oxidized Fe powder gain sufficient kinetic energy to overcome the binding forces in the oxide lattice to lead O atoms to escape from the NiFeW target. These ejected oxygen species are highly energetic, potentially causing further oxidation of other metal elements on a substrate [33]. Moreover, with a limited oxygen supply in an argon deposition atmosphere, a partially oxidized thin film is deposited to form the nonstoichiometric oxide of  $(\text{Fe}, \text{Ni}, \text{W})_3\text{O}_{4-x}$ , accompanied by the metallic alloy of Ni, Fe and W. This process for the NFW-oxide deposit introduces the multivalent metals of Ni, Fe, and W, and the oxide defects, specifically OV, as corroborated by XPS and EPR results.

### 3.2. Electrocatalytic performance

#### 3.2.1. Study on the $\text{NO}_3\text{RR}$ performance of sputtered NFW-n thin-film electrodes

The  $\text{NO}_3\text{RR}$  performance of various NFW-n thin films was assessed in an H-type electrolytic cell under ambient conditions, utilizing a 1 M

KOH solution with a 10 mM  $\text{KNO}_3$  aqueous solution as the electrolyte. As shown in Fig. 3a, linear sweep voltammetry (LSV) curves of NFW-n thin films in 1 M KOH electrolyte, with (dash line) and without (solid line)  $\text{NO}_3^-$ , were recorded to explore the potential window for the  $\text{NO}_3\text{RR}$  process. In comparison, the LSV curve of the single Ni and binary NiFe as the control samples exhibited poor cathodic activity. However, a remarkable enhancement in electrolytic reduction performance was observed in NFW-n samples. This improvement was evident as the polarization curve shifted to a lower potential, indicating the positive influence of W on the reduction activity of the ternary NiFeW-oxide thin film. Notably, NFW-0.5 demonstrated the highest electrocatalytic activity for  $\text{NO}_3\text{RR}$ , displaying the lowest overpotential and highest current density. Conversely, the single Ni and binary NiFe displayed negligible performance for  $\text{NO}_3\text{RR}$ , as indicated by the nearly unchanged current density after adding 10 mM  $\text{KNO}_3$ . Additionally,  $\text{NH}_3$  yield rates of NFW-n, NiFe, and Ni catalysts at a potential of -0.2 V vs. RHE and 10 mM  $\text{KNO}_3$  are presented in Fig. 3b. The highest  $\text{NH}_3$  yield rate of 13.8 mg/h.cm<sup>2</sup> was achieved on NFW-0.5 at a potential of -0.2 V vs. RHE, approximately 1.9, 2.74, 7.85 and 16.1 times higher than that of NFW-0.25, NFW-1, NiFe, and Ni at the same applied voltage, respectively. These results underscore the critical role of oxygen vacancies in contributing to the  $\text{NO}_3\text{RR}$  activity of as-deposited thin films. While NFW-1 exhibits the largest amount of OV, excessive oxygen vacancies can lead to trapped defects and structural instability [35]. This results in a lowered charge carrier density and induces extremely stable  $\text{H}_{\text{ad}}^*$  adsorption on the active sites [36], consequently decreasing the  $\text{NO}_3\text{RR}$  efficiency. It suggests that an optimum concentration of oxygen vacancies, neither too high nor too low, is necessary to achieve optimal electrocatalytic activity in NFW-0.5. Color-varying photo images of NFW-n after the 2 h  $\text{NO}_3\text{RR}$  test with the addition of the Nessler reagent are depicted in Fig. 3c. The observation is that the strongest orange color was visually observed for NFW-0.5 catalyst, confirming its superior ammonia productivity among NFW-n. The potential application of NFW-0.5 for ammonia production has been further demonstrated by its superior performance compared to several other as-developed alloy-/metal-oxide systems (Fig. S3). Our yield rate of 54.6 mg/h.cm<sup>2</sup> has made great enhancement.

To understand electron transport behavior, we conducted EIS tests for NFW-n, NiFe, and Ni in the (10 mM  $\text{KNO}_3$  + 1 M KOH) electrolyte. The experimental data were fitted using an equivalent circuit model inserted in Fig. 3d for the Nyquist plot. The electrochemical charge transfer resistance ( $R_{\text{ct}}$ ) for NFW-0.5 was determined to be 4.32  $\Omega$ —significantly smaller than its NFW-n counterparts: NFW-0.25 (7.34  $\Omega$ ), NFW-1 (8.13  $\Omega$ ), NiFe (12.32  $\Omega$ ), and Ni (12.97  $\Omega$ ). The more efficient charge transport mechanism for NFW-0.5 in enhancing  $\text{NO}_3\text{RR}$  activity performance, compared to single Ni or NiFe, may be attributed to the presence of defective  $\text{WO}_{3-x}$ . It has been reported that the presence of oxygen vacancies in  $\text{WO}_{3-x}$  can enhance electrical conductivity and facilitate electron transfer during the electrochemical process [37–39]. Moreover, the electrochemical active surface area (ECSA) of NFW-0.5 and NiFe was determined by the electrochemical double-layer capacitance (Fig. 3e and S4). The ECSA value of NFW-0.5 (222.5 cm<sup>2</sup>) is approximately 1.93 times higher than that of NiFe (115 cm<sup>2</sup>). The ECSA value is strongly related to the catalytically active site and the electrolytic activity of NFW-0.5 for  $\text{NO}_3\text{RR}$  in this work [6].

We further investigated the effect of the electrolyte environment on the  $\text{NO}_3\text{RR}$  performance of the NFW-0.5 catalyst. In comparing the LSV measurements of NFW-0.5 across different electrolytes (Fig. S5a), superior performance in the HER/ $\text{NO}_3\text{RR}$  reactions was observed in an alkaline medium compared to a neutral medium. It's noteworthy that in an alkaline electrolyte, the water dissociation step for proton supply occurs more rapidly in kinetics compared to a neutral medium [40], leading to a more sufficient supply of  $\text{H}_{\text{ad}}^*$  for  $\text{NO}_3^-$  reduction. Additionally, as illustrated in Fig. S5b-c, the charge transfer resistance of NFW-0.5 in 1 M KOH + 10 mM  $\text{KNO}_3$  was lower than that in other electrolyte environments. As anticipated, with an abundance of  $\text{H}_{\text{ad}}^*$

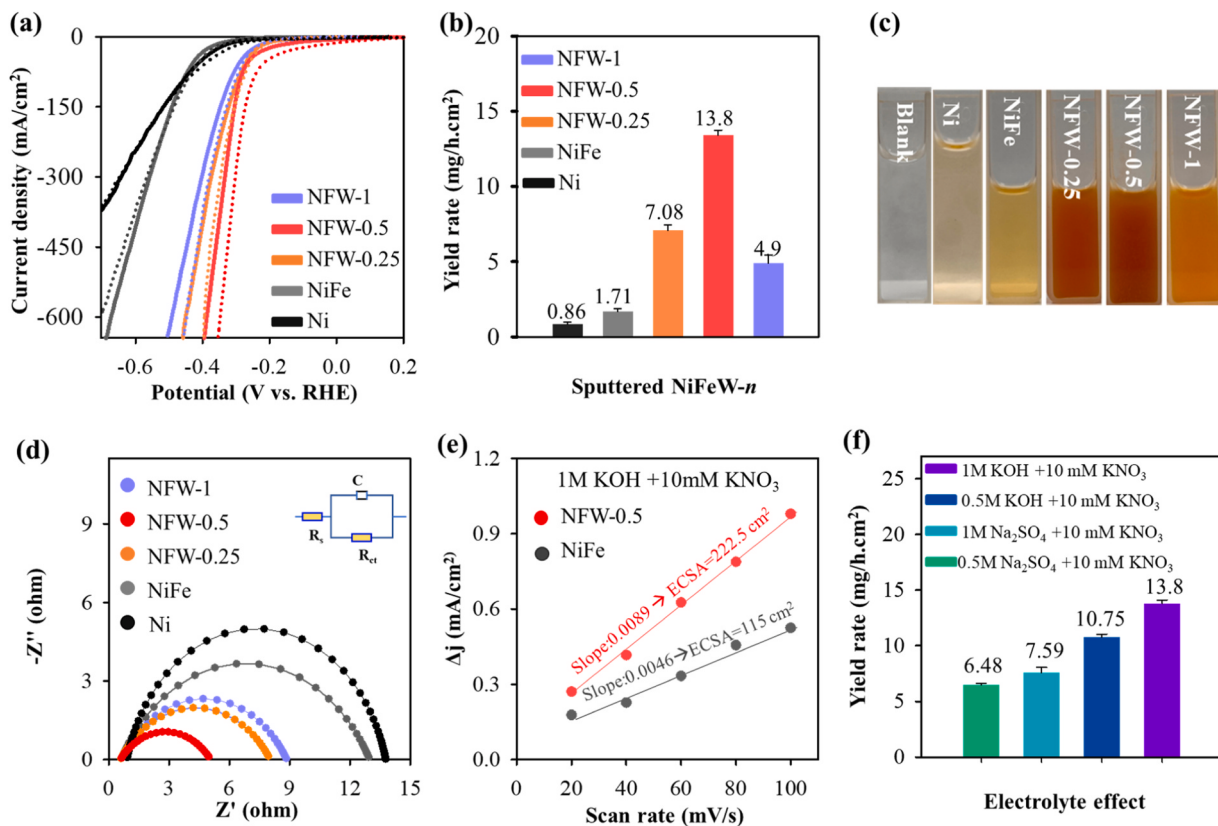


**Fig. 3.** Evaluations of different NFW-*n* (*n* = 0.25, 0.5, and 1), NiFe, and single Ni thin-film electrocatalytic electrodes for excellent NO<sub>3</sub>RR performance. (a) LSV tests in 1 M KOH (solid line) and 1 M KOH + 10 mM KNO<sub>3</sub> electrolyte (dash line). (b) The ammonia yield rate in (1 M KOH + 10 mM KNO<sub>3</sub>) at -0.2 V vs. RHE. (c) Color-varying photo images after 2 h NO<sub>3</sub>RR tests. (d) Nyquist plot. (e) The plot of current density vs. scan rate to estimate the double-layer capacitance (C<sub>dl</sub>). (f) Electrolyte effect

available and faster charge transfer in alkaline environments, the NH<sub>3</sub> yield rates operated at -0.2 V vs. RHE was approximately 10.75 mg/h.cm<sup>2</sup> in 0.5 M KOH and reached the highest value of 13.8 mg/h.cm<sup>2</sup> in 1 M KOH, while significantly lower values of 6.48 and 7.59 mg/h.cm<sup>2</sup> were observed in 0.5 M Na<sub>2</sub>SO<sub>4</sub> and 1 M Na<sub>2</sub>SO<sub>4</sub>, respectively (Fig. 3f).

### 3.2.2. Effects of the electrolyte concentration and applied potential on NO<sub>3</sub>RR

To investigate the optimal amount of NO<sub>3</sub> as a reactant, the ammonia production rate is evaluated in 1 M KOH with the varied KNO<sub>3</sub> concentration, ranging from 10 to 200 mM. As demonstrated in Fig. 4a, the outstanding electrocatalytic activity of NFW-0.5 for NO<sub>3</sub>RR was confirmed as the current density increased with the presence of NO<sub>3</sub> [41,42]. Additionally, the impact of NO<sub>3</sub> on ammonia yield rate is illustrated in Fig. 4b. The results revealed that the judicious electrolyte choice, specifically (100 mM KNO<sub>3</sub> + 1 M KOH), facilitated NFW-0.5 in exhibiting superior NO<sub>3</sub>RR performance, yielding 54.6 mg/h.cm<sup>2</sup> with a Faradaic efficiency of 93.7% at -0.2 V vs. RHE. Particularly, the lower NO<sub>3</sub> concentration markedly influenced ammonia yield rate, diminishing to 25.4 mg/h.cm<sup>2</sup> in 50 mM KNO<sub>3</sub> and further to 13.8 mg/h.cm<sup>2</sup> in 10 mM KNO<sub>3</sub>, due to a constrained supply of NO<sub>3</sub> [43,44]. With increasing KNO<sub>3</sub> concentration up to 200 mM, the NO<sub>3</sub>RR yield rate of NFW-0.5 was also impeded, as the excess NO<sub>3</sub> in the electrolyte potentially masked the catalyst's active sites and blocked the proton attachment, leading to a decrease in the NH<sub>3</sub> yield rate.

The results of NO<sub>3</sub>RR electrocatalysis at different applied potentials are presented in Fig. 4c. The NH<sub>3</sub> yield rates of NFW-0.5 are 24.5, 54.6, 47.6, and 49.5 mg/h.cm<sup>2</sup> at the applied potentials of -0.1, -0.2, -0.3, and -0.4 V, respectively, with their respective Faradaic efficiency values of 89.1, 93.7, 57.3, and 36.8%. The NFW-0.5 catalyst achieved the

highest yield rate of 54.6 mg/h.cm<sup>2</sup> at -0.2 V vs. RHE with a superior FE of 93.7%. Furthermore, the FE of NFW-0.5 for NO<sub>3</sub>RR exhibits a volcano-type trend as a function of applied potential, reaching a maximum value of 93.7% at -0.2 V vs. RHE and decreasing to 36.83% at -0.4 V vs. RHE. This phenomenon can be attributed to the increased competition from the hydrogen evolution reaction at more negative potentials i.e., < -0.2 V, coupled with fewer available charges at the more positive potential i.e., > -0.1 V [45,46].

To confirm the origin of NH<sub>3</sub> from the NO<sub>3</sub> reduction, a test in a blank 1 M KOH solution without NO<sub>3</sub> was performed (Fig. S6). No detection of NH<sub>3</sub> confirms that the obtained NH<sub>3</sub> is indeed derived from NO<sub>3</sub> reduction. Additionally, to mitigate detection deviations, we compared both the Nessler and the indophenol blue (IPB) colorimetric quantification methods. As shown in Fig. S7, the IPB results were consistent with the colorimetric NH<sub>3</sub> assay utilizing the Nessler reagent.

To further elucidate the enhanced selectivity and reaction kinetics of NFW-0.5 toward NO<sub>3</sub>RR, *operando* EIS measurements were conducted in two electrolytes: 1 M KOH and (1 M KOH + 100 mM KNO<sub>3</sub>). The experimental data underwent analysis by fitting them to an equivalent circuit model, as depicted in Fig. 4d-e for the Nyquist plot. The obtained charge transfer resistances were then documented in Table S2. In comparison to a pure KOH system, NFW-0.5 demonstrates lower resistance at various applied potentials in a (1 M KOH + 100 mM KNO<sub>3</sub>) electrolyte, aligning with its rapid ion kinetics in NO<sub>3</sub>RR, as evidenced by the LSV curves (Fig. 4a). In detail, in the 1 M KOH system, Nyquist spectra of NFW-0.5 exhibit nearly oblique lines at the open circuit potentials (OCP) and 0 V vs. RHE, indicating elevated resistance at the interface between the electrode and the electrolyte. When an applied potential exceeds -0.1 V vs. RHE, a conspicuous semicircle emerges with R<sub>ct</sub> of 16.8 Ω, signifying the onset of electrocatalytic HER. Conversely, EIS spectra of

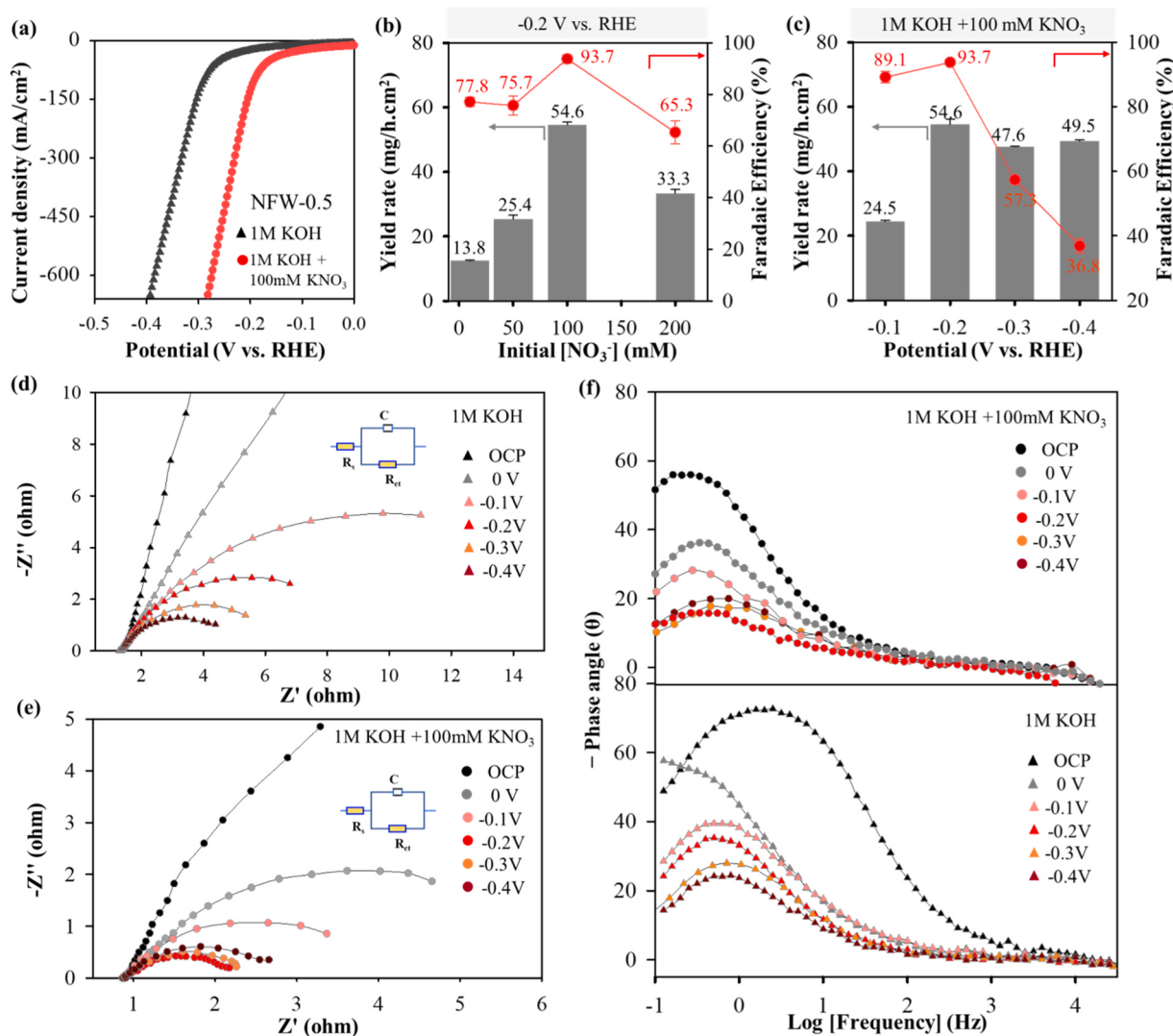


**Fig. 4.** (a) LSV curves of NFW-0.5 in 1 M KOH and (1 M KOH + 100 mM KNO<sub>3</sub>) electrolytes. Ammonia productivity as a function of (b) nitrate concentration and (c) applied potential, accompanied by their corresponding Faradaic efficiencies. Nyquist plots for NFW-0.5 at different applied potentials vs. RHE in (d) 1 M KOH and (e) 1 M KOH + 100 mM KNO<sub>3</sub>. (f) Bode phase plots of the NFW-0.5.

NFW-0.5 in the mixed electrolyte reveal a decreased semicircle diameter initially as the potential decreases from 0 vs. RHE ( $R_{ct} = 4.5 \Omega$ ) to  $-0.2$  V vs. RHE ( $R_{ct} = 1.34 \Omega$ ), followed by a gradual increase at  $-0.3$  V vs. RHE ( $R_{ct} = 1.42 \Omega$ ) and  $-0.4$  V vs. RHE ( $R_{ct} = 1.82 \Omega$ ). This higher impedance behavior suggests diminished kinetics in NO<sub>3</sub>RR due to competitive HER at higher potentials [14,47], aligning with experimental findings as shown in Fig. 4c. Furthermore, analyses of Bode phase plots (Fig. 4f) reveal that, as the potential varies from 0 to  $-0.4$  V vs. RHE, the lower phase angle at lower frequencies is observed in the (KOH + KNO<sub>3</sub>) system compared to pure KOH, indicative of lower resistance and enhanced ion diffusion capacity [48]. The phase peaks of NFW-0.5 at  $-0.3$  and  $-0.4$  V vs. RHE slightly shift to higher frequencies and exhibit higher phase angles than that at  $-0.2$  V vs. RHE, implying lower selectivity in NO<sub>3</sub>RR at applied potentials exceeding  $-0.2$  V vs. RHE [41].

### 3.2.3. Overall electrolytic nitrate reduction in a single NFW-0.5(+)|NFW-0.5(-) stack cell

Recently, despite the development of some promising catalysts for nitrate reduction reactions, all the experimental data have been tested in the H-cell configuration. To demonstrate the feasibility of overall nitrate electrolysis for large-scale ammonia synthesis, it is imperative to invest in efficient catalysts that exhibit good selectivity toward both NO<sub>3</sub>RR

and the OER to facilitate a comprehensive process. Drawing inspiration from the remarkable electrocatalytic activity of NFW-0.5 in NO<sub>3</sub>RR, we evaluated its OER performance to construct a comprehensive ammonia production cell. As illustrated in Fig. S8a-b, our NFW-0.5 exhibits excellent OER performance, requiring low overpotentials of 228, 348, and 460 mV to deliver high current densities of 100, 500, and 1000 mA/cm<sup>2</sup>, respectively. Even no notable increase in applied potential was observed over a continuous 50 h operation at an extremely high current density of 1000 mA/cm<sup>2</sup> (Fig. S8c). The remarkable consistency is evident in the nearly overlapping LSV curves before and after the stability operation at high current density (Fig. S8a), emphasizing the sustainable electrocatalytic OER performance of NFW-0.5.

The stack-cell setup for comprehensive nitrate reduction is illustrated in Fig. 5a, featuring various components such as two end plates, gaskets, a cathode, a membrane, and an anode. Gaskets were strategically positioned near the cathode and anode to establish an efficient gas- and liquid-tight seal. The bifunctional electrodes are separated by a Nafion membrane, facilitating the transport of proton ions. As shown in Fig. 5b, the NFW-0.5(+)|NFW-0.5(-) assembly demonstrates good efficiency for water splitting i.e., HER||OER with a low cell voltage of 1.90 and 1.97 V to deliver current densities of 100 and 500 mA/cm<sup>2</sup>, respectively. Notably, the cell voltage of NO<sub>3</sub>RR=|OER is reduced to

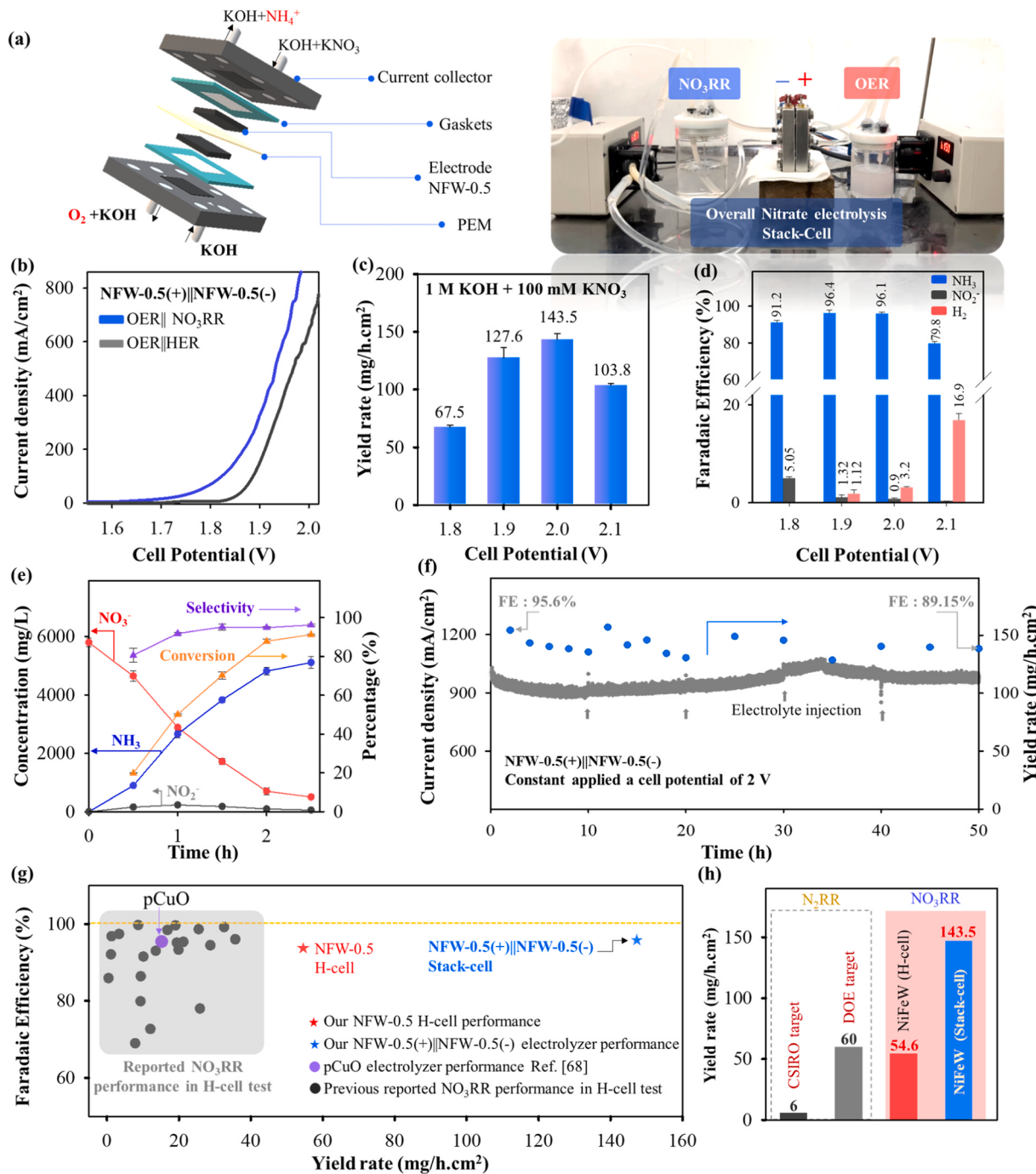


**Fig. 5.** (a) A schematic plot of the 4 cm<sup>2</sup> NFW-0.5(+)||NFW-0.5(−) electrolyzer for overall electrolytic nitrate reduction. (b) LSV curves for ammonia production using NFW-0.5 as both the cathode and anode. (c) The ammonia productivity as a function of applied cell voltage in 1 M KOH + 100 mM KNO<sub>3</sub>. (d) Faradaic efficiencies of generated products at different cell voltages. (e) Calculated ammonia selectivity, nitrate conversion, the amount of ammonia, and NO<sub>2</sub><sup>−</sup> formation as a function of time at 2.0 V in 1 M KOH + 100 mM KNO<sub>3</sub>. (f) Long-term electrocatalytic stability test for 50 h (gray arrows indicate the renewal of fresh electrolytes). (g) NO<sub>3</sub>RR performance of our NFW-0.5 H-type cell and NFW-0.5(+)||NFW-0.5(−) single stack cell in terms of ammonia yield rate and Faradaic efficiency, in comparison with the recently reported data. (h) Comparison of the NH<sub>3</sub> yield rates of our NFW-0.5-built cells with the set targets.

1.82 V @100 mA/cm<sup>2</sup> and 1.92 V @500 mA/cm<sup>2</sup>, indicating the enhancement effect of the nitrate-coupling electrolysis. Furthermore, the significant impact of the applied cell voltage on the NH<sub>3</sub> yield rate is clearly illustrated in Fig. 5c. The NH<sub>3</sub> yield rate initially increases rapidly as the potential rises, reaching 67.5 mg/h.cm<sup>2</sup> at 1.8 V and then escalating to 143.5 mg/h.cm<sup>2</sup> at 2.0 V. However, it begins to decrease to 103.8 mg/h.cm<sup>2</sup> at 2.1 V due to the competitive HER.

Considering the intricate nature of NO<sub>3</sub>RR, various potential byproducts may arise, including N<sub>2</sub>, H<sub>2</sub>, and NO<sub>2</sub><sup>−</sup>. Therefore, NO<sub>2</sub><sup>−</sup>

concentration was quantified using the UV-Vis colorimetric method, while gas chromatography was employed to analyze gas products throughout the reaction. Notably, the NFW-0.5(+)||NFW-0.5(−) electrolyzer did not exhibit detectable N<sub>2</sub> production. As depicted in Fig. 5d, applying a cell voltage of 1.8 V yielded a Faraday efficiency of 91.2% for NH<sub>3</sub> (FENH<sub>3</sub>) and 5.05% for NO<sub>2</sub><sup>−</sup> (FENO<sub>2</sub><sup>−</sup>), with no observed H<sub>2</sub> generation. Increasing the voltage to 2.0 V resulted in further enhancement of FENH<sub>3</sub> to 96.1%, accompanied by a reduction in FENO<sub>2</sub><sup>−</sup> to 0.9%. However, raising the cell potential to 2.1 V led to a decrease in FENH<sub>3</sub> to

79.8%, attributed to competitive HER activity, as Faraday efficiency of H<sub>2</sub> (FEH<sub>2</sub>) reached 16.9%. The progression of product yields over time under an applied cell voltage of 2.0 V in 1 M KOH + 100 mM KNO<sub>3</sub> is depicted in Fig. 5e. The kinetics of ammonia generation follow a nearly linear trend over the reaction duration, concurrent with a gradual reduction in the NO<sub>3</sub><sup>-</sup> concentration. NO<sub>2</sub> is observed to be generated at an early stage, potentially transforming into NH<sub>3</sub> with increased reaction time. Nitrate conversion reaches 18.9% after 30 min, steadily increasing to 90.6% over 2.5 h, with a remarkable ammonia selectivity of 97.6%, demonstrating the high performance of our electrolyzer. In the other hand, considering the actual discharge of nitrate concentrations from industrial sites, which can be 3000 mg/L [49], we conducted experiments with the NFW-0.5 (+)||NFW-0.5(-) electrolyzer using a lower KNO<sub>3</sub> concentration of 50 mM to assess practicality. As illustrated in Fig. S9a, an increase in the applied cell voltage from 1.8 to 2.0 V resulted in a rise in ammonia productivity from 53.9 mg/h.cm<sup>2</sup> to 83.9 mg/h.cm<sup>2</sup> with an FENH<sub>3</sub> of 95.8%. Further increments in the cell potential to 2.1 V inhibited the NO<sub>3</sub>RR, as evidenced by the increased competition with HER and a decrease in FENH<sub>3</sub> to 77.5%. The progression of product yields over time under an applied cell voltage of 2.0 V in 1 M KOH + 50 mM KNO<sub>3</sub> is depicted in Fig. S9b. Similar to observations with 100 mM KNO<sub>3</sub>, a nearly linear increase in ammonia production over reaction time was observed. Although a lower NH<sub>3</sub> production rate was noted with a decreased concentration of nitrate to 50 mM, a higher conversion rate of 97.1% of nitrate to ammonia was achieved, with a high ammonia selectivity of 96.9% after 2.5 h. These results suggest that our electrolyzer may be suitable for solutions with a range of nitrate concentrations.

For the reusability test, the continuous cycling tests at 2.0 V in 1 M KOH + 100 mM KNO<sub>3</sub> for our symmetrical NFW-0.5(+)||NFW-0.5(-) cell, illustrated in Fig. S10a, reveal variations in productivity rate and Faradaic efficiency within a reasonable range over continuous 10 cycles. The yield rate consistently exceeded 130 mg/h.cm<sup>2</sup> and FENH<sub>3</sub> maintained at about 90%. To evaluate the long-term stability for practical applications, we further conducted a chronoamperometry stability test on the electrolyzer, operating at an applied cell potential of 2.0 V in 1 M KOH + 100 mM KNO<sub>3</sub> for 50 h. As illustrated in Fig. 5f, the current density exhibited slight variations over the continuous 50 h operation. After 50 h, a minor decline in the electrocatalytic performance of NO<sub>3</sub>RR was observed, with the NH<sub>3</sub> yield rate decreasing to 138.24 mg/h.cm<sup>2</sup>, corresponding to an FENH<sub>3</sub> of 89.15%. The recorded LSV curves further indicated minimal degradation in the overall nitrate reduction activity before and after the stability tests (Fig. S10b), demonstrating the robustness of our bifunctional NFW-0.5 electrodes in facilitating both electrochemical NO<sub>3</sub>RR and OER. Furthermore, chloride (Cl<sup>-</sup>) is a common halide ion that may be present in natural water at concentrations of up to 5 mM [50]. Therefore, we investigated the effects of co-existing Cl<sup>-</sup> ions on the electrochemical reduction of nitrate at initial chloride concentrations of 1 mM and 5 mM. As shown in Fig. S11, our electrolyzer exhibited lower NO<sub>3</sub>RR performance in the presence of Cl<sup>-</sup>, with an ammonia productivity of 138.12 mg/h.cm<sup>2</sup> when 1 mM Cl<sup>-</sup> was introduced, which decreased to 125.86 mg/h.cm<sup>2</sup> at 5 mM Cl<sup>-</sup>. The efficiency at 87.36% remains comparable to a Cl<sup>-</sup>-free condition. This decrease in the rate performance may be attributed to the competitive adsorption of chloride on the catalyst surface, along with insufficient H<sub>ad</sub>\* generation, resulting in a reduced NO<sub>3</sub>RR activity [51].

A file containing the experimental process of overall water electrolysis and overall nitrate electrolysis is documented in Video S1. It is observed that, under an applied cell potential of 2.0 V, numerous bubbles are generated at both the HER and OER cells, corresponding to the production of hydrogen gas and oxygen gas, respectively. However, upon introducing NO<sub>3</sub><sup>-</sup> for the overall nitrate electrolysis process, bubbles disappear at the NO<sub>3</sub>RR end, suggesting that the majority of hydrogen species enriched on the electrocatalyst may have been involved in the hydrogenation process of NO<sub>3</sub><sup>-</sup> instead of HER [52]. This observation aligns with the high FENH<sub>3</sub> of 96.1% achieved by our NFW-0.5(+)||NFW-0.5(-) electrolyzer. Remarkably, the NO<sub>3</sub>RR was

conducted within a flow stack-cell configuration, resulting in a significantly increased NH<sub>3</sub> yield rate compared to the H-cell experiment. This improvement can be attributed to the longer duration for soluble NO<sub>3</sub><sup>-</sup> to pass through an extended active channel in a reaction cell. However, one NO<sub>3</sub><sup>-</sup> ion in an H-type cell has a lesser opportunity to be adsorbed on a cathode, i.e., the NO<sub>3</sub><sup>-</sup> chemical has difficulty in re-adsorption on active sites for further reactions, so the H-type cell faces challenges related to various electrolyte concentration throughout extended testing periods. The utilization of a continuous flow electrolyzer can help in mitigating performance degradation caused by mass transfer limitations [53].

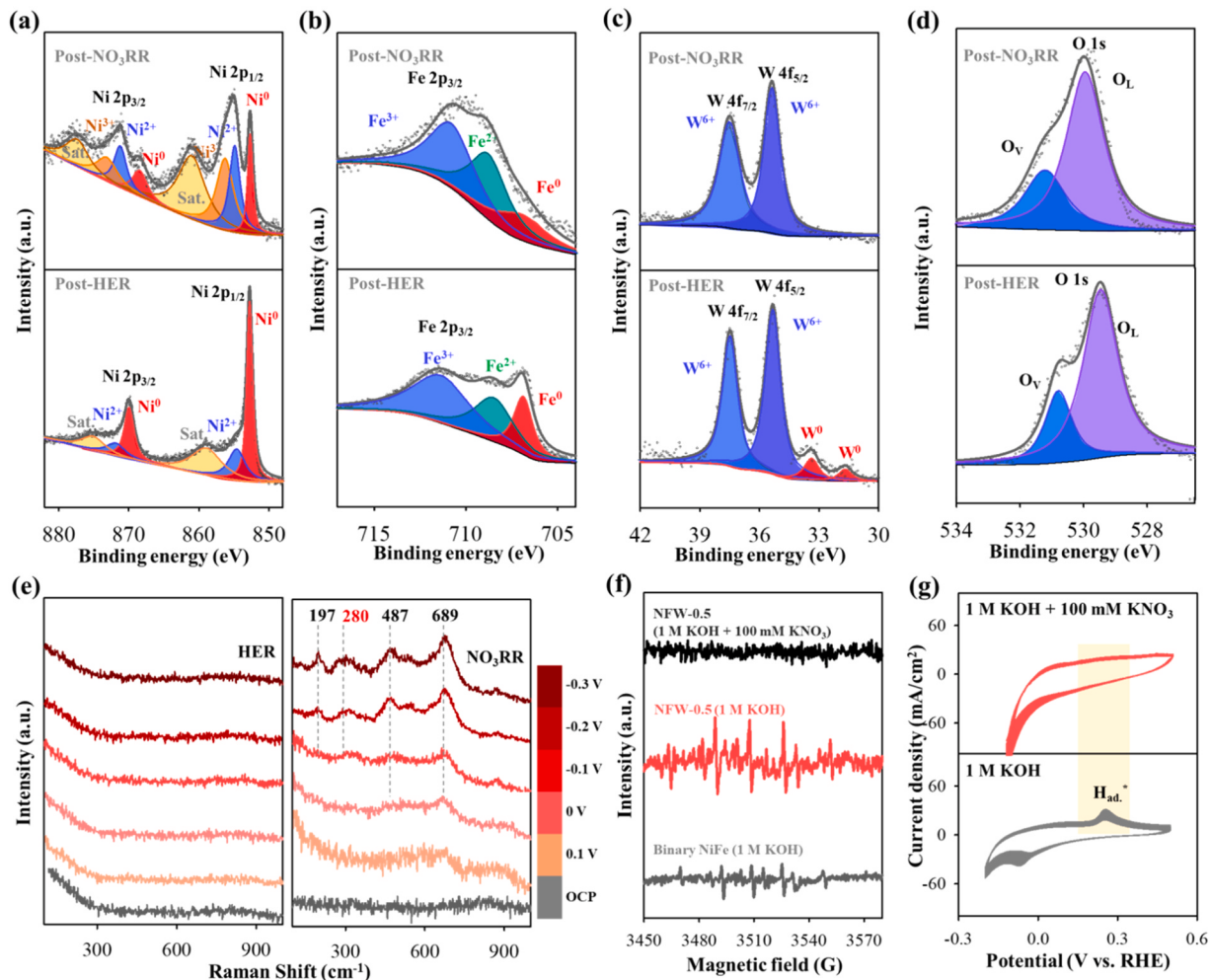
Supplementary material related to this article can be found online at doi:10.1016/j.apcatb.2024.124137.

Fig. 5g and Table S3 provide a comprehensive comparison of NH<sub>3</sub> yield rate and Faradaic efficiency among our NFW-0.5 H-cell, NFW-0.5 (+)||NFW-0.5(-) electrolyzer constructed with bifunctional NFW-0.5 electrodes, and other reported NO<sub>3</sub>RR results. Notably, our sputtered NFW-0.5 thin-film electrocatalyst outperforms most recently developed catalysts e.g., metal alloy, metal oxide, and metal phosphide produced through traditional synthesis methods, such as chemical reaction, hydrothermal method, and electrodeposition. Specifically, NFW-0.5 exhibits an outstanding yield rate of up to 54.6 mg/h.cm<sup>2</sup> for a nitrate-to-ammonia conversion in H-cell tests at -0.2 V vs. RHE, while reaching 143.5 mg/h.cm<sup>2</sup> at 2.0 V in the stack-cell tests (Fig. 5h). This electrolyzer also exhibits a low energy consumption of 26.3 kWh/kg.NH<sub>3</sub> and an energy efficiency of 26%, referring to the detailed computation provided in the supporting information. It is noteworthy that, until now, there has been limited discussion regarding the energy efficiency and energy consumption aspects in the context of electrocatalysts for NO<sub>3</sub>RR, as most reports investigate only the cathodic reduction in H-type electrolytic cells. The calculation of the cell efficiency for NO<sub>3</sub>RR performance necessitates the applied cell voltage in a 2-electrode system with both electrodes being equally important. In this regard, our bifunctional NiFeW-0.5 cell stands out as an energy-efficient device for ammonia production.

### 3.3. Post-characterizations and electrocatalytic mechanism

The morphological property and valence states of NFW-0.5 before and after the NO<sub>3</sub>RR process were investigated through SEM and XPS. As shown in Fig. S12, no significant changes in the morphology of NFW-0.5 after post-NO<sub>3</sub>RR were observed, indicating its stability and feasibility for NO<sub>3</sub>RR. However, Ni 2p XPS revealed a noteworthy decrease in the presence of Ni<sup>0</sup> species in NFW-0.5 after post-NO<sub>3</sub>RR (Fig. 6a). The emergence of peaks at 873.0 eV (Ni<sup>2+</sup> 2p<sub>1/2</sub>), 875.2 eV (Ni<sup>3+</sup> 2p<sub>1/2</sub>), 855.1 eV (Ni<sup>2+</sup> 2p<sub>3/2</sub>), and 856.6 eV (Ni<sup>3+</sup> 2p<sub>3/2</sub>) indicates a significant coexistence of Ni<sup>2+</sup> and Ni<sup>3+</sup>. The ratio of Ni<sup>0</sup>: Ni<sup>2+</sup>: Ni<sup>3+</sup> changed from 1: 0.2: 0-1: 1.6: 1.9. Furthermore, as shown in Fig. 6b, the slight change in the Fe 2p XPS spectra with an intensity-lower Fe<sup>0</sup> peak after post-NO<sub>3</sub>RR indicates the increase of the Fe<sup>2+</sup> and Fe<sup>3+</sup> contents together or the continuous oxidation of surface Fe metal. The calculated ratio of Fe<sup>0</sup>: Fe<sup>2+</sup>: Fe<sup>3+</sup> changed from 0.248: 0.370: 0.382-0.200: 0.390: 0.410. The XPS analysis of the W 4p regions (Fig. 6c) revealed the complete oxidation of W metal to a higher 6+ oxidation state on the surface of NFW-0.5 after post-NO<sub>3</sub>RR. In the O 1s high-resolution spectrum of NFW-0.5 after post-NO<sub>3</sub>RR (Fig. 6d), a noticeable decrease in the relative percentage of OV's was observed, decreasing from 36.3% to 29.2% for NFW-0.5. The lower content of OV's in NiFeW after cycling tests demonstrates clear evidence of the strong interaction between the catalyst and NO<sub>3</sub><sup>-</sup> species in forming weakly oxidized M-O bonds via the aid of OV's as the active sites to promote the NO<sub>3</sub>RR. Contrary to post-NO<sub>3</sub>RR, the XPS analysis of post-HER NFW-0.5 revealed that the characteristic high-resolution XPS peaks of Ni 2p, Fe 2p, W 4f, and O 1s are remarkably similar to those of the initial NFW-0.5, indicating no discernible change in oxidation states after the HER process.

To investigate the active components involved in the nitrate reduction process, *in-situ* Raman spectroscopy of NFW-0.5 was performed in



**Fig. 6.** High-resolution XPS spectra of (a) Ni 2p, (b) Fe 2p, (c) W 4f, and (d) O 1s for NFW-0.5 after the NO<sub>3</sub>RR (post-NO<sub>3</sub>RR), and after the HER (post-HER). (e) *In-situ* Raman of NFW-0.5 in 1 M KOH and 100 mM KNO<sub>3</sub> + 1 M KOH during cathodic polarization from 0.1 to −0.3 V vs. RHE. (f) EPR spectra of NiFe and NFW-0.5 using DMPO as the radical trapping reagent. (g) Cyclic voltammograms obtained with NFW-0.5 in 1 M KOH with and without KNO<sub>3</sub> with a scan rate of 20 mV/s.

1 M KOH and 1 M KOH + 100 mM KNO<sub>3</sub> electrolytes. As depicted in Fig. 6e, spectra were collected at various applied potentials ranging from 0.1 V to −0.3 V vs. RHE. At open circuit potential, no Raman signal was detected for NFW-0.5, consistent with the amorphous nature observed by XRD. During HER in 1 M KOH, no obvious difference was observed for the spectra obtained at the open circuit potential and various applied potentials, indicating that no significant phase transformation occurred during the HER process for NFW-0.5, as evidenced by XPS (the bottom plot in Fig. 6a-d). In the case of the NO<sub>3</sub>RR process, as the working potential decreased from 0.1 V to −0.1 V vs. RHE, signals appeared at 197, 487, and 689 cm<sup>-1</sup>, which can be assigned to metal–oxygen (M–O) bonds such as Ni–O and Fe–O [54,55]. Besides, a broad peak centered at 280 cm<sup>-1</sup> is attributed to the W–O–W bending mode vibration [56,57]. As the applied potential shifted more negatively to −0.2 and −0.3 V vs. RHE, clear evidence of the formation of M–O bonds was observed, typically caused by oxynitride species adsorbed on the catalyst's surface during the NO<sub>3</sub>RR process [58]. The results are consistent with the XPS data (the top plot in Fig. 6a-d), which indicate partial oxidation of Ni, Fe, and W after the post-NO<sub>3</sub>RR process.

The introduction of OVs in electrocatalysts through multivalent metal substitution has been observed to significantly modulate adsorption energies for intermediates of reactants on the catalyst surface [45, 59]. This phenomenon effectively lowers the energy barrier associated with the electroreduction of NO<sub>3</sub><sup>−</sup> to NH<sub>3</sub> while concurrently impeding the formation of undesirable by-products [60]. Additionally, the

presence of OVs induces a shift in the d-band center of active metal sites to optimal energy levels, thereby serving as the primary sites for nitrate adsorption and subsequent ammonia desorption [61]. It is crucial to note that the dissociation of H<sub>2</sub>O plays an important role in initiating the NO<sub>3</sub>RR process, involving the generation and consumption of the active hydrogen intermediate[62]. To explore the role of oxygen vacancies in the generation of active hydrogen radicals, EPR measurements were conducted using 5,5-dimethyl-1-pyrroline-N-oxide (DMPO) as an H-capturing reagent for both NiFe and NFW-0.5 catalysts (Fig. 6f). In the absence of nitrate, DMPO-H signals were detected for both NiFe and NFW-0.5, indicating the presence of H<sub>ad</sub><sup>+</sup>. However, NFW-0.5 displayed more intense DMPO-H signals compared to NiFe, suggesting that the presence of largely defective oxygen, obtained by substituting W into NiFe, promotes hydrolysis dissociation and enhances H<sub>ad</sub><sup>+</sup> formation. In the existence of nitrate, the DMPO-H signals of NFW-0.5 disappeared, indicating its exceptional ability to rapidly consume H<sub>ad</sub><sup>+</sup> during the NO<sub>3</sub>RR process. Previous reports have highlighted that the presence of OVs enhances the generation of H<sub>ad</sub><sup>+</sup> through the Volmer step [59]. Consequently, a sufficient supply of H<sub>ad</sub><sup>+</sup> substantially facilitates the conversion of intermediate products into ammonia, ultimately leading to a high ammonia yield rate [63]. The sufficient generation of active H<sub>ad</sub><sup>+</sup> on our NFW-0.5 was further intuitively verified by cyclic voltammetry. As depicted in Fig. 6g, in the 1 M KOH electrolyte, NFW-0.5 exhibits an oxidation peak at approximately 0.3 V vs. RHE, indicative of H<sub>ad</sub><sup>+</sup> generation [64]. However, this signal disappears in 1 M KOH +

100 mM KNO<sub>3</sub>, suggesting the conversion of NO<sub>3</sub><sup>-</sup> to NH<sub>3</sub> in the NO<sub>3</sub>RR process, which leads to the consumption of H<sub>ad.</sub>\*. These results confirm that the ability to generate and consume H<sub>ad.</sub>\* plays a crucial role in enhancing the NO<sub>3</sub>RR performance of the NFW-0.5 catalyst.

In the detailed reaction mechanism for our NFW-0.5 (Fig. 7, Step 1), the OV sites, presented as V<sub>O</sub><sup>2+</sup> in a doubly positively charged state, are surrounded by metal cations. Before the start of applying potential, these electron-deficient V<sub>O</sub><sup>2+</sup> sites have been pre-occupied by absorbing O<sup>2-</sup> of OH<sup>-</sup>/H<sub>2</sub>O from the alkaline environment to form (HO)<sub>O,ad.</sub><sup>+</sup>, as illustrated in Eq. 1. Based on Eqs. 2–3, V<sub>O</sub><sup>2+</sup> attracts negatively charged oxygen in H<sub>2</sub>O to create (H<sub>2</sub>O)<sub>O,ad.</sub><sup>2+</sup>, which, in turn, generates H<sub>ad.</sub>\* through the Volmer step with the electrons supplied from the applied voltage. Subsequently, the produced H<sub>ad.</sub>\* is employed to deoxygenate NO<sub>3</sub><sup>-</sup>, while the regenerated V<sub>O</sub><sup>2+</sup> sites in Eq. 3 can be used as the H<sub>ad.</sub>\*-generating sources for NO<sub>3</sub>RR to continuously proceed. If H<sub>ad.</sub>\* recombines to form H<sub>2</sub> via the HER pathway, it diminishes the availability of H<sub>ad.</sub>\* for subsequent steps of NO<sub>3</sub>RR, potentially constraining overall ammonia production efficiency. Thus, in our NFW-0.5 catalyst, as demonstrated by EPR DMPO-H and CV tests, the ample supply of H<sub>ad.</sub>\* from water splitting and its timely utilization by NO<sub>3</sub>RR intermediates might be pivotal in achieving high NH<sub>3</sub> production efficiency with elevated FENH<sub>3</sub>.

From the post-XPS analysis and *in-situ* Raman, we understand that the NiFeW-0.5 electrode, though used as a cathode for the reduction reaction, undergoes the oxidation reaction itself to form the multivalent cations of Ni<sup>2+/3+</sup>, Fe<sup>2+/3+</sup>, and W<sup>6+</sup> in its lattice. The electrons in the unpaired d-orbitals for those cations can help the electrons flowing from the external power supply through NiFeW-0.5 then to the catalyst

surface for the reduction reaction in Eq. 3. The electron transfer pathway in electrocatalysts during the NO<sub>3</sub>RR process is illustrated as the Step 2 in Fig. 7, where electrons transport *via* hopping along the cation sites and ultimately reaching the catalyst/electrolyte interface for the reaction. An example of this hopping mechanism can be expressed as an equation of Ni<sup>2+</sup> + Fe<sup>3+</sup>  $\xrightarrow{e^-}$  Ni<sup>3+</sup> + Fe<sup>2+</sup>. As the hopping mechanism has hinted, the lower electrode resistance can be achieved by defect engineering in forming more multivalent metal cations on the catalyst lattice for a shorter hopping distance. The superior electron transport property of NFW-0.5 was previously evidenced by EIS, as depicted in Fig. 3d. Previous studies have also found that the introduction of OVs contributes to the formation of high-spin metal oxide active sites. These catalytic sites provide electrons in the e<sub>g</sub> orbital with a higher energy state, facilitating the NO<sub>3</sub><sup>-</sup> reduction catalyzed by the M<sup>r+</sup>-M<sup>(r+1)+</sup>-M<sup>r+</sup> redox cycle [65].

It's noteworthy that ammonia conversion from nitrate involves two widely accepted pathways: indirect reduction, accomplished by electrons and H<sup>+</sup>, and direct reduction, triggered by atomic H<sub>ad.</sub>\* [66,67]. Our experiments above confirm that H<sub>ad.</sub>\* predominantly facilitates the direct reduction of NO<sub>3</sub> to NH<sub>3</sub> by our NFW-0.5 (\*NO<sub>3</sub><sup>-</sup>  $\rightarrow$  \*NO<sup>-</sup>  $\rightarrow$  \*N  $\rightarrow$  \*NH<sub>3</sub>  $\rightarrow$  NH<sub>3</sub>). The mechanism of nitrate electroreduction is presented as Step 3 in Fig. 7. This NO<sub>3</sub>RR reaction initiates with the chemical absorption of NO<sub>3</sub> on the OV site (Eq. 4) by oxidizing the surrounding multivalent cations to share the electrons from O in NO<sub>3</sub> for forming the M-O bond with the cations to its higher oxidation state, i.e. Ni<sup>2+</sup>  $\rightarrow$  Ni<sup>3+</sup> and Fe<sup>2+</sup>  $\rightarrow$  Fe<sup>3+</sup>. The OV site is the trapping/pinning center to induce oxidative adsorption, as this site is surrounded by 4

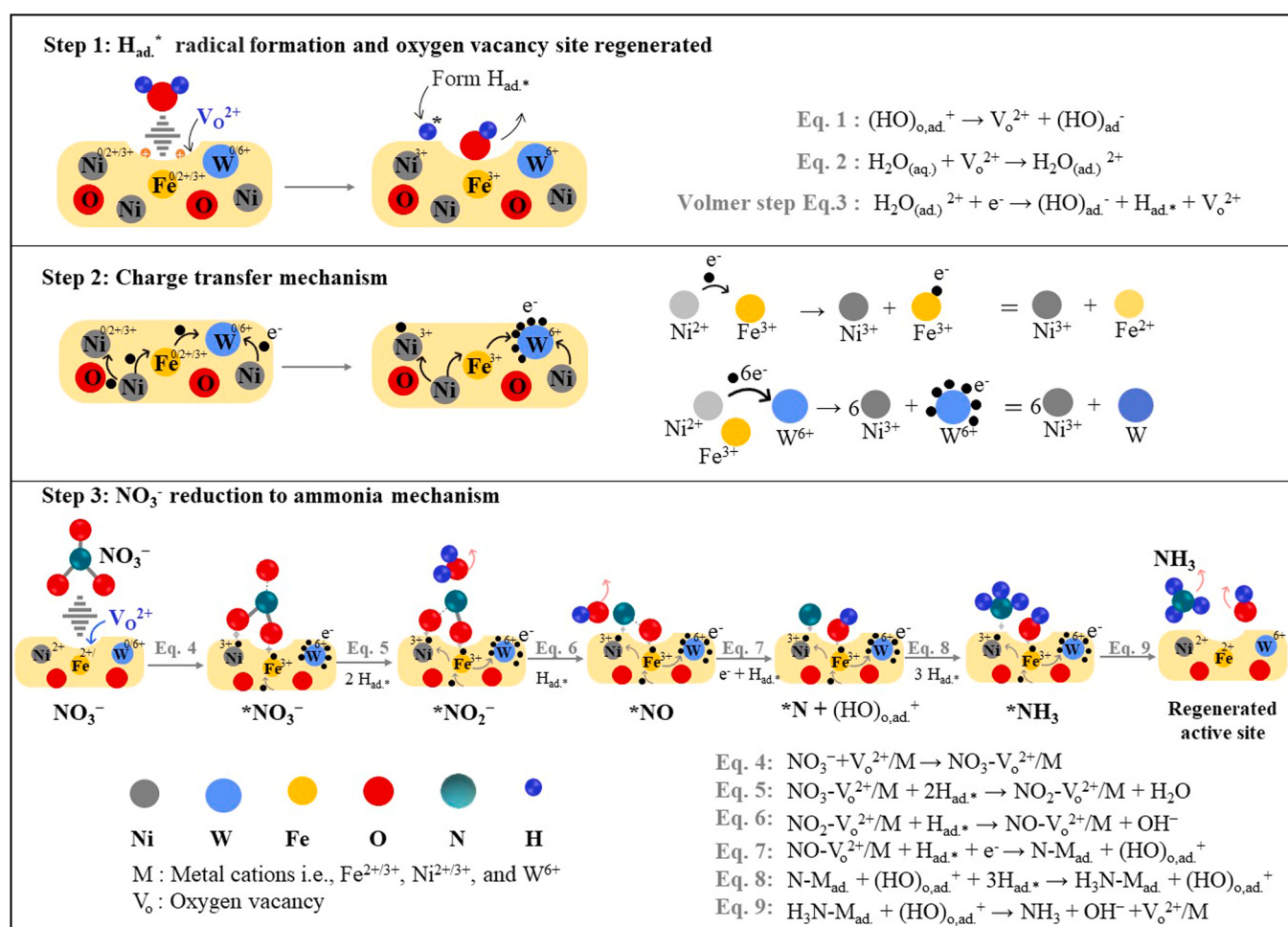


Fig. 7. Schematic representations of the three steps in explaining the NO<sub>3</sub>RR reaction mechanism on the surface of NFW-0.5.

cations in an octahedral skeleton of  $(\text{Fe}, \text{Ni})_3\text{O}_{4-x}$  spinel for example. The surface cations around OV can physically or weakly adsorb the O of  $\text{NO}_3^-$  without chemical reaction, as there is only one cation for interaction. With the strongly fixed  $\text{NO}_3^-$  at one end by an OV pinning center, the pinned  $\text{NO}_3^-$  can have a long residence time for the hydrodeoxygenation reaction step by step (Eq. 5-Eq.8) to form the  $\text{NH}_3$ . Once the pinned nitrogen leaves the electrode (Eq. 9) by replacing it with the  $\text{OH}^-$  group to resume the Eq. 1 reaction, the cations around the pinning centers lower their valence states back to the initial stage for preparing the next oxidative adsorption of  $\text{NO}_3^-$ .

The goal for the electrocatalytic nitrogen reduction ( $\text{N}_2\text{RR}$ ) for  $\text{NH}_3$  has been set with the yield rates reaching  $6 \text{ mg}/\text{h.cm}^2$  for the Commonwealth Scientific and Industrial Research Organisation (CSIRO) target and  $60 \text{ mg}/\text{h.cm}^2$  for the Department of Energy (DOE) one [68], while  $\text{NO}_3\text{RR}$ , an easier reaction due to a polar and liquid reactant, has not been set yet. As shown in Fig. 5h, our NFW-0.5(+)||NFW-0.5(−) cell with a yield rate of  $143.5 \text{ mg}/\text{h.cm}^2$  for  $\text{NO}_3\text{RR}$  is excellent for the green conversion. The basic performance for a cell to be industrialized needs to reach a current density of  $300 \text{ mA}/\text{cm}^2$ , 90% Faradaic efficiency, and long-term stability. Our 250 nm-thick NiFeW-0.5 catalyst made by the magnetron sputtering thin-film technology is expected to have the strongest adherence to the Ni foam substrate without the catalyst-peeling problem due to the plasma-assisted deposition. Our NFW-0.5(+)||NFW-0.5(−) cell with the strongly adherent and bifunctional catalyst, reaching a current density of  $900 \text{ mA}/\text{cm}^2$  at  $2.0 \text{ V}$ , a Faradaic efficiency of 96.1%, 26% energy efficiency, and energy consumption of  $26.3 \text{ kWh/kg.NH}_3$ , has great potential for industrialization.

#### 4. Conclusions

A ternary NiFeW-oxide thin-film electrode was successfully fabricated using the magnetron sputtering thin-film technique. Our sputtered NFW-0.5 catalyst with a thickness of 250 nm and a uniform composition distribution was in an amorphous state and demonstrated exceptional performance in nitrate reduction with ammonia productivity of  $54.6 \text{ mg}/\text{h.cm}^2$  at  $-0.2 \text{ V}$  vs. RHE and a Faradaic efficiency of 93.7%. This performance surpasses most of the currently reported electrocatalysts developed through traditional methods such as hydrothermal and electrodeposition. XPS and EPR revealed the formation of metallic alloy of Ni, Fe, and W, and the partially oxidized  $(\text{Fe}, \text{Ni}, \text{W})_3\text{O}_{4-x}$  spinel doped with Ni and W. The catalyst contains multivalent  $\text{Ni}^{2+/3+}$ ,  $\text{Fe}^{2+/3+}$ , and  $\text{W}^{6+}$  at cation lattices and the oxygen vacancies at the anion sites to establish the fast charge-transport hopping channel and surface active sites for  $\text{NO}_3\text{RR}$ . Feasibility studies for overall nitrite electrolysis using a  $2 \times 2 \text{ cm}^2$  single stack cell NFW-0.5(+)||NFW-0.5(−) indicate that a low cell voltage of  $2.0 \text{ V}$  has shown to achieve a remarkable  $\text{NH}_3$  yield rate of  $143.5 \text{ mg}/\text{h.cm}^2$  with 96.1% Faradaic efficiency, energy efficiency of 26%, and low energy consumption of  $26.3 \text{ kWh/kg.NH}_3$ . To explain the excellent catalysis, an oxygen vacancy-based  $\text{NO}_3^-$ -pinned mechanism is proposed to have O in  $\text{NO}_3^-$  be fixed by the oxidative adsorption for the following speedy hydrodeoxygenation reaction to form  $\text{NH}_3$ . This study introduces an innovative approach to designing highly efficient and strongly adhered bifunctional thin-film electrocatalysts capable of achieving an efficient stack cell for the industrialization of  $\text{NO}_3\text{RR}$ .

#### CRediT authorship contribution statement

**Merga Hailemariam Urgesa:** Visualization, Investigation. **Wen-Chuan Hsiao:** Methodology, Investigation, Formal analysis. **Dong-Hau Kuo:** Writing – review & editing, Supervision, Funding acquisition, Conceptualization. **Quoc-Nam Ha:** Writing – original draft, Visualization, Supervision, Methodology. **Tadele Negash Gemedo:** Visualization, Investigation. **Chan-Yu Chan:** Investigation, Formal analysis.

#### Declaration of Competing Interest

The authors declare that they have no known competing financial interests or personal relationships that could have appeared to influence the work reported in this paper.

#### Data availability

Data will be made available on request.

#### Acknowledgments

This work was supported by the National Science and Technology Council (NCST), Taiwan, under grant numbers MOST-110-2221-E-011-038-MY3 and MOST 110-2221-E-011-100-MY3. Thanks to Precious Instrumentation Center at NTUST for ULVAC PHI 5000 VersaProbe III XPS analysis.

#### Appendix A. Supporting information

Supplementary data associated with this article can be found in the online version at doi:10.1016/j.apcatb.2024.124137.

#### References

- [1] B. Timmer, W. Olthuis, A. Van Den Berg, Ammonia sensors and their applications—a review, *Sens. Actuators B: Chem.* 107 (2005) 666–677.
- [2] M. Wang, M.A. Khan, I. Mohsin, J. Wicks, A.H. Ip, K.Z. Sumon, C.-T. Dinh, E. H. Sargent, I.D. Gates, M.G. Kibria, Can sustainable ammonia synthesis pathways compete with fossil-fuel based Haber–Bosch processes, *Energy Environ. Sci.* 14 (2021) 2535–2548.
- [3] T.N. Gameda, D.-H. Kuo, Q.-N. Ha, One-step synthesized  $\text{Nb}_2\text{O}_5-\gamma$ -decorated spinel-type  $(\text{Ni}, \text{V})_3\text{O}_{4-x}$  nanoflowers for boosting electrocatalytic reduction of nitrogen into ammonia, *Green. Chem.* 25 (2023) 10498–10512.
- [4] G. Qing, R. Ghazfar, S.T. Jackowski, F. Habilizadeh, M.M. Ashiani, C.-P. Chen, M. R. Smith III, T.W. Hamann, Recent advances and challenges of electrocatalytic  $\text{N}_2$  reduction to ammonia, *Chem. Rev.* 120 (2020) 5437–5516.
- [5] P.H. van Langevelde, I. Katsounaros, M.T. Koper, Electrocatalytic nitrate reduction for sustainable ammonia production, *Joule* 5 (2021) 290–294.
- [6] Y. Wang, A. Xu, Z. Wang, L. Huang, J. Li, F. Li, J. Wicks, M. Luo, D.-H. Nam, C.-S. Tan, Enhanced nitrate-to-ammonia activity on copper–nickel alloys via tuning of intermediate adsorption, *J. Am. Chem. Soc.* 142 (2020) 5702–5708.
- [7] J. Lim, C.-Y. Liu, J. Park, Y.-H. Liu, T.P. Senftle, S.W. Lee, M.C. Hatzell, Structure sensitivity of Pd facets for enhanced electrochemical nitrate reduction to ammonia, *ACS Catal.* 11 (2021) 7568–7577.
- [8] H. Liu, J. Park, Y. Chen, Y. Qiu, Y. Cheng, K. Srivastava, S. Gu, B.H. Shanks, L. T. Roling, W. Li, Electrocatalytic nitrate reduction on oxide-derived silver with tunable selectivity to nitrite and ammonia, *ACS Catal.* 11 (2021) 8431–8442.
- [9] D. Hao, Y. Wei, L. Mao, X. Bai, Y. Liu, B. Xu, W. Wei, B.-J. Ni, Boosted selective catalytic nitrate reduction to ammonia on carbon/bismuth/bismuth oxide photocatalysts, *J. Clean. Prod.* 331 (2022) 129975.
- [10] R. Brunet, L. Garcia-Gil, Sulfide-induced dissimilatory nitrate reduction to ammonia in anaerobic freshwater sediments, *FEMS Microbiol. Ecol.* 21 (1996) 131–138.
- [11] D. Liu, L. Qiao, S. Peng, H. Bai, C. Liu, W.F. Ip, K.H. Lo, H. Liu, K.W. Ng, S. Wang, Recent advances in electrocatalysts for efficient nitrate reduction to ammonia, *Adv. Funct. Mater.* 33 (2023) 2303480.
- [12] T. Chouki, M. Machreki, I.A. Rutkowska, B. Rytlewska, P.J. Kulesza, G. Tyuliev, M. Harb, L.M. Azofra, S. Emin, Highly active iron phosphide catalysts for selective electrochemical nitrate reduction to ammonia, *J. Environ. Chem. Eng.* 11 (2023) 10975.
- [13] R. Zhang, Y. Guo, S. Zhang, D. Chen, Y. Zhao, Z. Huang, L. Ma, P. Li, Q. Yang, G. Liang, Efficient ammonia electrosynthesis and energy conversion through a  $\text{Zn}$ -nitrate battery by iron doping engineered nickel phosphide catalyst, *Adv. Energy Mater.* 12 (2022) 2103872.
- [14] D. Liu, L. Qiao, Y. Chen, P. Zhou, J. Feng, C.C. Leong, K.W. Ng, S. Peng, S. Wang, W.F. Ip, Electrocatalytic reduction of nitrate to ammonia on low-cost manganese-incorporated  $\text{Co}_3\text{O}_4$  nanotubes, *Appl. Catal. B: Environ.* 324 (2023) 122293.
- [15] X.-H. Wang, Z.-M. Wang, Q.-L. Hong, Z.-N. Zhang, F. Shi, D.-S. Li, S.-N. Li, Y. Chen, Oxygen-vacancy-rich  $\text{Cu}_2\text{O}$  hollow nanocubes for nitrate electroreduction reaction to ammonia in a neutral electrolyte, *Inorg. Chem.* 61 (2022) 15678–15685.
- [16] S. Li, C. Xiao, R. Chen, M. Wang, Y. Ma, K. Luo, M. Shen, Y. Zhu, Y. Li, C. Li, Near 100% selectivity for ammonia synthesis at a high current density by promoting nitrate protonation on the copper dispersed todorokite-type manganese oxide, *Green. Chem.* 25 (2023) 10549–10555.

[17] S. Meng, Y. Ling, M. Yang, X. Zhao, A.I. Osman, H. Ala'a, D.W. Rooney, P.-S. Yap, Recent research progress of electrocatalytic reduction technology for nitrate wastewater: a review, *J. Environ. Chem. Eng.* (2023) 109418.

[18] X. Liu, C. Liu, X. He, Z. Cai, K. Dong, J. Li, X. Fan, T. Xie, X. Yang, Y. Luo, Fe-doped  $\text{Co}_3\text{O}_4$  nanowire struttet 3D pinewood-derived carbon: a highly selective electrocatalyst for ammonia production via nitrate reduction, *Nano Res.* (2023) 1–7.

[19] W. Jung, Y.J. Hwang, Material strategies in the electrochemical nitrate reduction reaction to ammonia production, *Mater. Chem. Front.* 5 (2021) 6803–6823.

[20] C. Wang, Y. Zhang, H. Luo, H. Zhang, W. Li, Wx Zhang, J. Yang, Iron-based nanocatalysts for electrochemical nitrate reduction, *Small Methods* 6 (2022) 2200790.

[21] J. Wang, S. Xin, Y. Xiao, Z. Zhang, Z. Li, W. Zhang, C. Li, R. Bao, J. Peng, J. Yi, Manipulating the water dissociation electrocatalytic sites of bimetallic nickel-based alloys for highly efficient alkaline hydrogen evolution, *Angew. Chem. Int. Ed.* 61 (2022) e202202518.

[22] Z. He, J. Zhang, Z. Gong, H. Lei, D. Zhou, N. Zhang, W. Mai, S. Zhao, Y. Chen, Activating lattice oxygen in NiFe-based (oxy) hydroxide for water electrolysis, *Nat. Commun.* 13 (2022) 2191.

[23] Y. Li, J. Ma, Z. Wu, Z. Wang, Direct electron transfer coordinated by oxygen vacancies boosts selective nitrate reduction to  $\text{N}_2$  on a Co–CuO<sub>x</sub> electroactive filter, *Environ. Sci. Technol.* 56 (2022) 8673–8681.

[24] R.A. Nickell, W.H. Zhu, R.U. Payne, D.R. Cahela, B.J.J. Jops Tatarchuk, Hg/HgO electrode and hydrogen evolution potentials in aqueous sodium hydroxide, 161 (2006) 1217–1224.

[25] J. Sun, B. Yu, F. Tan, W. Yang, G. Cheng, Z. Zhang, High throughput preparation of Ni–Mo alloy thin films as efficient bifunctional electrocatalysts for water splitting, *Int. J. Hydrog. Energy* 47 (2022) 15764–15774.

[26] L. Fan, P.F. Liu, X. Yan, L. Gu, Z.Z. Yang, H.G. Yang, S. Qiu, X. Yao, Atomically isolated nickel species anchored on graphitized carbon for efficient hydrogen evolution electrocatalysis, *Nat. Commun.* 7 (2016) 10667.

[27] Q.-N. Ha, N.S. Gultom, C.-H. Yeh, D.-H. Kuo, One-pot synthesized Li, V co-doped  $\text{Ni}_3\text{S}_2$  nanorod arrays as a bifunctional electrocatalyst for industrialization-facile hydrogen production via alkaline exchange membrane water electrolysis, *Chem. Eng. J.* 472 (2023) 144931.

[28] Z. Hou, P. Yan, B. Sun, H. Elshekh, B. Yan, An excellent soft magnetic Fe/Fe<sub>3</sub>O<sub>4</sub>/FeSiAl composite with high permeability and low core loss, *Results Phys.* 14 (2019) 102498.

[29] P.L. Tran-Nguyen, A.E. Angkawijaya, Q.N. Ha, Y.N. Tran-Chuong, A.W. Go, V. Bundajaya, C. Gunarto, S.P. Santoso, Y.-H. Ju, Facile synthesis of superparamagnetic thiamine/Fe<sub>3</sub>O<sub>4</sub> with enhanced adsorptivity toward divalent copper ions, *Chemosphere* 291 (2022) 132759.

[30] K.D. Wright, A.R. Barron, Catalyst residue and oxygen species inhibition of the formation of hexahapto-metal complexes of group 6 metals on single-walled carbon nanotubes, *C* 3 (2017) 17.

[31] W. Pan, M. Cao, C. Diao, C. Tao, H. Hao, Z. Yao, Z. Yu, H. Liu, Structures and dielectric properties of (Nb, Zn) co-doped SrTiO<sub>3</sub> ceramics at various sintering temperatures, *J. Mater. Sci.* 54 (2019) 12401–12410.

[32] N.S. Gultom, Y.-C. Zhou, D.-H. Kuo, A facile and efficient method for preparing La-doped Co<sub>3</sub>O<sub>4</sub> by electrodeposition as an efficient air cathode in rechargeable zinc-air batteries: role of oxygen vacancies, *J. Colloid Interface Sci.* 655 (2024) 394–406.

[33] Q.-N. Ha, C.-H. Yeh, N.S. Gultom, D.-H. Kuo, Industrial-scale efficient alkaline water electrolysis achieved with sputtered NiFeV-oxide thin film electrodes for green hydrogen production, *J. Mater. Chem. A* 12 (2024) 460–474.

[34] Q.-N. Ha, N.S. Gultom, M.Z. Silitonga, T.N. Gemedo, D.-H. Kuo, Novel core-shell structure of  $\text{Ni}_3\text{S}_2@\text{LiMoNiO}_x(\text{OH})_y$  nanorod arrays toward efficient high-current-density hydrogen evolution reaction, *Chem. Eng. J.* 467 (2023) 143253.

[35] S. Corby, L. Francas, A. Kafizas, J.R. Durrant, Determining the role of oxygen vacancies in the photoelectrocatalytic performance of WO<sub>3</sub> for water oxidation, *Chem. Sci.* 11 (2020) 2907–2914.

[36] Z. Wu, T. Liao, S. Wang, J.A. Mudiyanselage, A.S. Micallef, W. Li, A.P. O'Mullane, J. Yang, W. Luo, K. Ostríkov, Conversion of catalytically inert 2D bismuth oxide nanosheets for effective electrochemical hydrogen evolution reaction catalysis via oxygen vacancy concentration modulation, *Nano-Micro Lett.* 14 (2022) 90.

[37] S. Cong, Y. Yuan, Z. Chen, J. Hou, M. Yang, Y. Su, Y. Zhang, L. Li, Q. Li, F. Geng, Noble metal-comparable SERS enhancement from semiconducting metal oxides by making oxygen vacancies, *Nat. Commun.* 6 (2015) 7800.

[38] C. Xie, W. Chen, S. Du, D. Yan, Y. Zhang, J. Chen, B. Liu, S. Wang, In-situ phase transition of WO<sub>3</sub> boosting electron and hydrogen transfer for enhancing hydrogen evolution on Pt, *Nano Energy* 71 (2020) 104653.

[39] K.-H. Kim, H. Lee, X. Huang, J.H. Choi, C. Chen, J.K. Kang, D. O'Hare, Energy-efficient electrochemical ammonia production from dilute nitrate solution, *Energy Environ. Sci.* 16 (2023) 663–672.

[40] Y. Xu, C. Wang, Y. Huang, J. Fu, Recent advances in electrocatalysts for neutral and large-current-density water electrolysis, *Nano Energy* 80 (2021) 105545.

[41] D. Zhu, G. Li, X. Yan, C. Geng, L. Gao, Electrochemical nitrate reduction to high-value ammonia on two-dimensional molybdenum carbide nanosheets for nitrate-containing wastewater upcycling, *Sci. Total Environ.* 878 (2023) 163145.

[42] H. Jiang, G.F. Chen, O. Savateev, J. Xue, L.X. Ding, Z. Liang, M. Antonietti, H. Wang, Enabled efficient ammonia synthesis and energy supply in a zinc-nitrate battery system by separating nitrate reduction process into two stages, *Angew. Chem. Int. Ed.* 62 (2023) e202218717.

[43] J. Wang, C. Cai, Y. Wang, X. Yang, D. Wu, Y. Zhu, M. Li, M. Gu, M. Shao, Electrocatalytic reduction of nitrate to ammonia on low-cost ultrathin CoO<sub>x</sub> nanosheets, *ACS Catal.* 11 (2021) 15135–15140.

[44] J. Liang, Q. Liu, A.A. Alshehri, X. Sun, Recent advances in nanostructured heterogeneous catalysts for N-cycle electrocatalysis, *Nano Res. Energy* 1 (2022) e9120010.

[45] K. Chu, W. Zong, G. Xue, H. Guo, J. Qin, H. Zhu, N. Zhang, Z. Tian, H. Dong, Y.-E. Miao, Cation substitution strategy for developing perovskite oxide with rich oxygen vacancy-mediated charge redistribution enables highly efficient nitrate electroreduction to ammonia, *J. Am. Chem. Soc.* 145 (2023) 21387–21396.

[46] Z. Wang, S.D. Young, B.R. Goldsmith, N. Singh, Increasing electrocatalytic nitrate reduction activity by controlling adsorption through PtRu alloying, *J. Catal.* 395 (2021) 143–154.

[47] X. Zhu, S. Mou, Q. Peng, Q. Liu, Y. Luo, G. Chen, S. Gao, X. Sun, Aqueous electrocatalytic  $\text{N}_2$  reduction for ambient NH<sub>3</sub> synthesis: recent advances in catalyst development and performance improvement, *J. Mater. Chem. A* 8 (2020) 1545–1556.

[48] X. Chen, Q. Wang, Y. Cheng, H. Xing, J. Li, X. Zhu, L. Ma, Y. Li, D. Liu, S-doping triggers redox reactivities of both iron and lattice oxygen in FeOOH for low-cost and high-performance water oxidation, *Adv. Funct. Mater.* 32 (2022) 2112674.

[49] P. Cyplik, M. Mareck, A. Piotrowska-Cyplik, A. Olejnik, A. Drozdzynska, L. Chrzanowski, Biological denitrification of high nitrate processing wastewaters from explosives production plant, *Water, Air, Soil Pollut.* 223 (2012) 1791–1800.

[50] M. Tang, Q. Tong, Y. Li, R. Jiang, L. Shi, F. Shen, Y. Wei, Z. Liu, S. Liu, J. Zhang, Effective and selective electrocatalytic nitrate reduction to ammonia on urchin-like and defect-enriched titanium oxide microparticles, *Chin. Chem. Lett.* 34 (2023) 108410.

[51] D. Richards, S.D. Young, B.R. Goldsmith, N. Singh, Electrocatalytic nitrate reduction on rhodium sulfide compared to Pt and Rh in the presence of chloride, *Catal. Sci. Technol.* 11 (2021) 7331–7346.

[52] J. Li, H. Li, K. Fan, J.Y. Lee, W. Xie, M. Shao, Electrocatalytic nitrate reduction to ammonia coupled with organic oxidation, *Chem. Catal.* 3 (2023).

[53] M. Yang, B. Li, S. Li, Q. Dong, Z. Huang, S. Zheng, Y. Fang, G. Zhou, X. Chen, X. Zhu, Highly selective electrochemical nitrate to ammonia conversion by dispersed Ru in a multielement alloy catalyst, *Nano Lett.* 23 (2023) 7733–7742.

[54] N. Dalai, B. Mohanty, A. Mitra, B. Jena, Highly active ternary nickel–iron oxide as bifunctional catalyst for electrochemical water splitting, *ChemistrySelect* 4 (2019) 7791–7796.

[55] W. Wang, Z. Ding, X. Zhao, S. Wu, F. Li, M. Yue, J.P. Liu, Microstructure and magnetic properties of  $\text{MFe}_2\text{O}_4$  ( $\text{M} = \text{Co}, \text{Ni}$ , and Mn) ferrite nanocrystals prepared using colloid mill and hydrothermal method, *J. Appl. Phys.* 117 (2015).

[56] M. Daniel, B. Desbat, J. Lassegués, B. Gerand, M. Figlarz, Infrared and Raman study of WO<sub>3</sub> tungsten trioxides and  $\text{WO}_3 \cdot x\text{H}_2\text{O}$  tungsten trioxide hydrates, *J. Solid State Chem.* 67 (1987) 235–247.

[57] L. Xu, M.-L. Yin, S. Liu, Agx@WO<sub>3</sub> core-shell nanostructure for LSP enhanced chemical sensors, *Sci. Rep.* 4 (2014) 6745.

[58] J.-Y. Fang, Q.-Z. Zheng, Y.-Y. Lou, K.-M. Zhao, S.-N. Hu, G. Li, O. Akdim, X.-Y. Huang, S.-G. Sun, Ampere-level current density ammonia electrochemical synthesis using CuCo nanosheets simulating nitrite reductase bifunctional nature, *Nat. Commun.* 13 (2022) 7899.

[59] N. Yao, R. Meng, F. Wu, Z. Fan, G. Cheng, W. Luo, Oxygen-Vacancy-Induced CeO<sub>2</sub>/Co<sub>4</sub>N heterostructures toward enhanced pH-Universal hydrogen evolution reactions, *Appl. Catal. B: Environ.* 277 (2020) 119282.

[60] H. Zheng, Y. Zhang, Y. Wang, Z. Wu, F. Lai, G. Chao, N. Zhang, L. Zhang, T. Liu, Perovskites with enriched oxygen vacancies as a family of electrocatalysts for efficient nitrate reduction to ammonia, *Small* 19 (2023) 2205625.

[61] S. Ullah, S. Wang, M.S. Ahmad, H.M.A. Sharif, Q. Liu, T. Kida, A. Shafique, M. U. Rehman, G. Wang, J. Qiu, Investigating the role of oxygen vacancies in metal oxide for enhanced electrochemical reduction of NO<sub>3</sub><sup>-</sup> to NH<sub>3</sub>: mechanistic insights, *Inorg. Chem. Front.* 10 (2023) 6440–6448.

[62] S. Zhang, J. Wu, M. Zheng, X. Jin, Z. Shen, Z. Li, Y. Wang, Q. Wang, X. Wang, H. Wei, Fe/Cu diatomic catalysts for electrochemical nitrate reduction to ammonia, *Nat. Commun.* 14 (2023) 3634.

[63] H. Luo, S. Li, Z. Wu, Y. Liu, W. Luo, W. Li, D. Zhang, J. Chen, J. Yang, Modulating the active hydrogen adsorption on Fe–N interface for boosted electrocatalytic nitrate reduction with ultra-long stability, *Adv. Mater.* 35 (2023) 2304695.

[64] K. Fan, W. Xie, J. Li, Y. Sun, P. Xu, Y. Tang, Z. Li, M. Shao, Active hydrogen boosts electrochemical nitrate reduction to ammonia, *Nat. Commun.* 13 (2022) 7958.

[65] Y. Chen, J. He, H. Pang, P. Jiang, F. Qu, D. Yu, J. Zhang, New insight into electrochemical denitrification using a self-organized nanoporous VO-Co<sub>3</sub>O<sub>4</sub>/Co cathode: Plasma-assistant oxygen vacancies catalyzed efficient nitrate reduction, *Sci. Total Environ.* 850 (2022) 157845.

[66] S. Garcia-Segura, M. Lanzarini-Lopes, K. Hristovski, P. Westerhoff, Electrocatalytic reduction of nitrate: fundamentals to full-scale water treatment applications, *Appl. Catal. B: Environ.* 236 (2018) 546–568.

[67] Z. Wu, Y. Song, H. Guo, F. Xie, Y. Cong, M. Kuang, J. Yang, Tandem catalysis in electrocatalytic nitrate reduction: unlocking efficiency and mechanism, *Interdiscip. Mater.* (2024).

[68] R. Daiyan, T. Tran-Phu, P. Kumar, K. Iputera, Z. Tong, J. Leverett, M.H.A. Khan, A. Esmailpour, A. Jalili, M. Lim, Nitrate reduction to ammonium: from CuO defect engineering to waste NO<sub>x</sub>-to-NH<sub>3</sub> economic feasibility, *Energy Environ. Sci.* 14 (2021) 3588–3598.